Surface & Coatings Technology 523 (2026) 133203

Contents lists available at ScienceDirect

Surface & Coatings Technology

journal homepage: www.elsevier.com/locate/surfcoat

Adhesion of DLC-based coatings on LPBF Al-Si-Mg alloys: influence of substrate hardness

Maria Francesca Bonilauri [a], Emanuele Ghio [b,*], Giovanni Bolelli [a,c,d], Bertè Alessandro [e], Emanuela Cerri [b]

[a] Department of Engineering "Enzo Ferrari", University of Modena and Reggio Emilia, Via Pietro Vivarelli 10/1, 41125 Modena (MO), Italy
[b] Department of Engineering for Industrial Systems and Technologies, University of Parma, Via G. Usberti 181/A, 43124, Parma, Italy
[c] InterMech MO.RE. Centro Interdipartimentale per la Ricerca Applicata e i Servizi nel Settore della Meccanica Avanzata e della Motoristica, University of Modena and Reggio Emilia, Via Pietro Vivarelli 2, 41125, Modena, Italy
[d] Consorzio Interuniversitario Nazionale per la Scienza e Tecnologia dei Materiali (INSTM), Local Unit: Università di Modena e Reggio Emilia, Via Pietro Vivarelli 10/1, 41125, Modena, Italy
[e] LAFER S.p.A., Strada Di Cortemaggiore 31, 29122, Piacenza, Italy

ARTICLE INFO

Keywords:
Diamond like carbon (DLC)
Additively manufactured Al-Si-Mg alloys
Heat treatment
Sliding wear
Scratch adhesion
Hardness

ABSTRACT

The microstructure and mechanical properties of Laser-Powder Bed Fusion (LPBF)-manufactured Al alloys can be tailored through heat treatments. To study how this affects the mechanical support offered to DLC-based thin films, we studied the adhesion of a DLC-based coating onto LPBF AlSi7Mg and AlSi10Mg alloys in four different conditions: as-built, directly aged, solution-treated, and T6 (solutionized and aged). Notably, the solution-treated substrates were harder than the T6 ones after coating due to precipitation during the deposition process itself, whilst the T6 substrates experienced over-aging.

The fraction of delaminated coating area in the Rockwell indentation test increased and the delamination load in the scratch test decreased when the heat treatment reduced the hardness of the substrate and altered the eutectic Si network produced by the LPBF process. During ball-on-disc sliding wear tests, all substrates, including the as-built ones, deformed plastically under the contact stress. The DLC top layer, with its high H/E ratio, could follow such deformation, but the underlying W-C:H intermediate layer cracked and caused localized spallation of the film, with increased severity on softer substrates. If the wear track passed through an open pore on the LPBF substrate, the additional stress concentration produced an even larger spallation or, with the directly aged or solutionized substrates, a complete delamination. Thus, a softened substrate, coupled with the typical defects of LPBF materials, worsened the repeatability of the sliding behaviour. After the T6 treatment, further reduction in hardness caused the film to delaminate systematically under the chosen test conditions.

1. Introduction

Diamond-Like Carbon (DLC) films are amorphous mixtures of sp^2- and sp^3-hybridized carbon and, often, some amount of hydrogen. Depending on hydrogen content and sp^3 fraction, DLC can be classified as hydrogen-free amorphous carbon (a-C), hydrogenated amorphous carbon (a-C:H), or tetrahedral amorphous carbon (ta-C), the latter being characterized by a very high sp^3 content and no hydrogen [1]. The sp^3 content confers very high hardness, usually around or above 2000 HV, and unlike a polycrystalline diamond film, the absence of crystalline grains results in a very smooth surface [2]. DLC films usually follow the substrate profile without introducing much additional roughness, apart from occasional clusters that result from vacuum deposition processes like Physical and Plasma-Assisted Chemical Vapour Deposition (PVD, PA-CVD) [1,3,4]. The a-C:H also have a very low surface energy because the dangling bonds of the surface carbon atoms are saturated by hydrogen [3–6]. This, together with their tendency to release a transfer film made of graphite and polymeric hydrocarbon chains on the counterpart, minimizes the adhesive component of friction when sliding against many types of counterparts. Thus, under vacuum conditions, ultra-low friction is frequently observed. In air, some oxygen and -OH groups also intervene to replace the H atoms: the friction coefficient

* Corresponding author.
E-mail addresses: mariafrancesca.bonilauri@unimore.it (M.F. Bonilauri), emanuele.ghio@unipr.it (E. Ghio), giovanni.bolelli@unimore.it (G. Bolelli), berte@lafer.eu (B. Alessandro), emanuela.cerri@unipr.it (E. Cerri).

https://doi.org/10.1016/j.surfcoat.2026.133203
Received 11 June 2025; Received in revised form 12 January 2026; Accepted 17 January 2026
Available online 19 January 2026

Table I
Nominal chemical composition (wt%) of both AlSi7Mg and AlSi10Mg alloys.

Alloys	Al	Si	Mg	Mn	Fe	Cu	Zn
AlSi7Mg	Bal.	7.05	0.59	0.005	0.07	< 0.005	0.011
AlSi10Mg		9.89	0.30	0.006	0.12	0.001	0.002

Table II
Temperature and duration of the solution heat treatment, the direct and the artificial aging treatments in peak-aging conditions.

HT conditions		AlSi7Mg		AlSi10Mg	
Direct aging (DA)		175 °C - 1 h		175 °C - 8 h	
T6	SHT	505 °C - 0.5 h	505 °C - 4 h	505 °C - 0.5 h	505 °C - 4 h
	Artificial aging (AA)	175 °C - 8 h	175 °C - 2 h	175 °C - 8 h	175 °C - 4 h

rises, but it usually stays at moderate levels of ~ 0.1–0.2 when sliding against common metallic or ceramic counterparts [1,3,4,6,7].

Because of these features, DLC films are employed to enhance the sliding wear performance of a variety of tribosystems, reducing friction under dry or boundary lubrication conditions and preventing wear in mechanical parts such as gears, valves, pins, cams, rockers, etc. [6,8–10], as well as in other application areas like biomedical parts [10,11]. With a thickness typically in the range of a few micrometres, they are especially useful for small-sized, precision parts, which can also be processed cost-effectively in batch-type PVD and/or PA-CVD systems.

In this context, two important trends have recently been emerging, which pose some peculiar challenges to DLC films. The first is the increasing tendency to use Al- and Ti-based alloys in a number of applications, most prominently the automotive and aerospace sectors, to take advantage of their high strength/density and stiffness/density ratios to achieve a reduction in mass and (in case of moving parts) inertia [12,13]. Aluminium and titanium alloys are softer than quenched-and-tempered steels and usually exhibit poorer resistance to sliding wear [14,15]. This means that they are in particular need for surface coatings [15,16], but these mechanical characteristics also constitute a significant issue for the application of a DLC film. In fact, the contact stress distribution under usual engineering conditions cannot be borne entirely by a micrometre-thin film. The sub-surface stress maximum is generally expected to fall into the substrate. Thus, if the substrate is more elastically and plastically compliant than the film, the latter can be compelled to follow a larger elastic or elastic-plastic deformation than it can accept, resulting in crack propagation within the film and along the film/substrate interface [17–21].

A recent study by the present authors [22] highlighted that DLC-based films, i.e. multi-layered systems ending with a DLC top layer, can crack and delaminate when deposited on LPBF-manufactured Ti-6Al-4 V, if too severe contact stress concentrations are induced by the application of large normal loads and/or by an excessively rough substrate surface. The problem could become even worse with Al alloy substrates, since they are softer than Ti alloys. A common solution that is often proposed is to produce duplex coatings, where a hard and thick underlayer improves the load-carrying ability of the softer substrate and supports the thin, hard and more brittle top layer [16]. For example, Di Egidio et al. [23,24] recently showed that a DLC-based film applied onto an AlSi10Mg substrate can withstand substantially higher contact pressures with the interposition of an electroless Ni(P) interlayer, some tens of micrometres thick. The interlayer, which has higher hardness and stiffness than the Al alloy substrate, takes on a substantial share of the contact stress, deforming less than the bare substrate and avoiding stress concentration in the DLC film itself. However, in general a duplex treatment increases the overall complexity and cost of the process, since it requires the use of two distinct technologies (e.g., electroless deposition and PVD/PA-CVD).

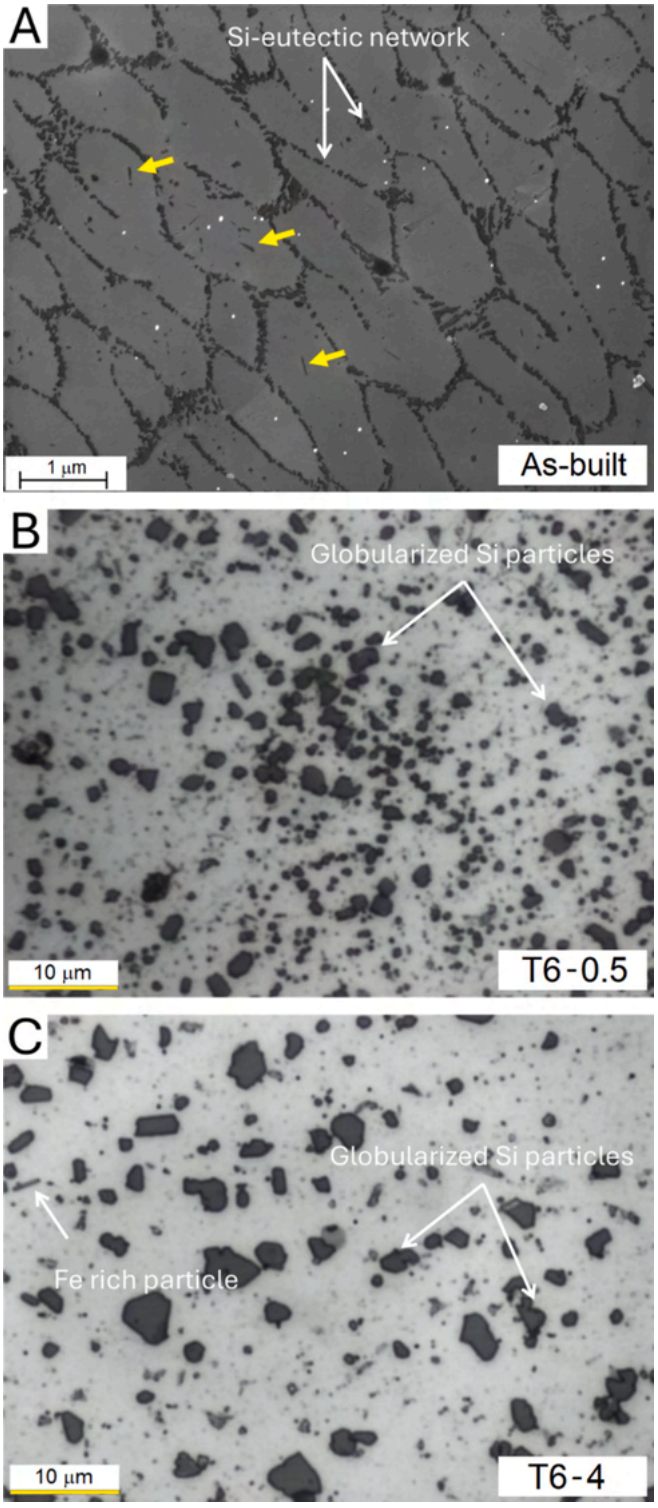

Fig. 1. Microstructures of Al-Si-Mg samples in AB (A) and T6 (B—C) conditions, where the SHT times was 0.5 h (B) and 4 h (C). Yellow arrows (A) indicate rod- and circle-shaped Si-nanoparticles.

The second important trend is the increasing market share of additive manufacturing (AM) technologies [25,26]. AM is especially useful to produce the kind of small-sized precision parts which, as mentioned above, are often coated by DLC-based films. The industrial usage of AM technologies is spurred by their distinctive advantages: near-net-shape manufacturing, which minimizes material wastage, and geometrical

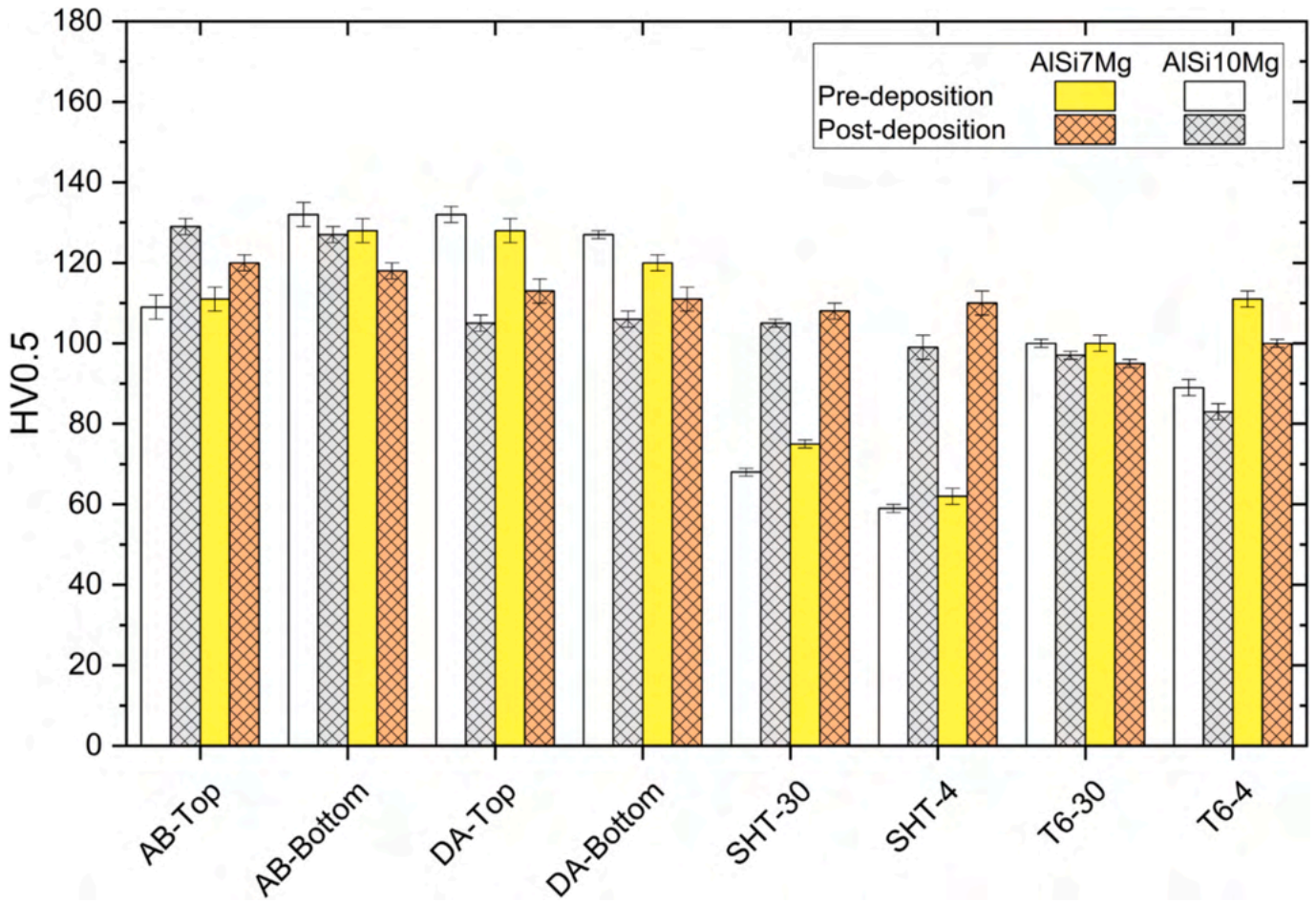

Fig. 2. Hardness variation of Al-Si-Mg substrates before and after the exposure to the DLC deposition temperature.

Table III
Dimensions of both α-Al cells and Si-eutectic network in AlSi7Mg and AlSi10Mg before and after exposure to 175 °C for 8 h.

	AlSi10Mg		AlSi7Mg	
	As-built	Direct-aged	As-built	Direct-aged
α-Al cells [nm]	612 ± 38	595 ± 45	587 ± 40	546 ± 50
Si-eutectic network [nm]	65 ± 20	69 ± 17	70 ± 10	70 ± 18

flexibility, which allows unprecedented design freedom, unattainable with conventional processing methods like machining, casting, or plastic deformation [25,26]. Therefore, coating deposition on additively manufactured parts is becoming more and more common, and this trend is likely bound to continue in the near future.

Laser-powder bed fused (L-PBFed) parts typically have a rather coarse surface finish, with as-built roughness values (Ra / Sa) around or above 10 μm [27]. Because a hard DLC-based film would suffer unacceptable concentrations of contact stress if applied on an excessively rough surface [17], finishing is mandatorily needed. The effect of the eventual roughness of a finished L-PBF part on the tribological performance of DLC-based films was investigated in our previous work on Ti-6Al-4 V parts cited above [22], as well as in other works, including on Al-alloy substrates [28]. The results clearly show that, in general, smooth substrates improve the practical adhesion of DLC-based films and their resistance to sliding and abrasive wear, because the contact stress peaks localized on the asperities are reduced. For example, in our previous work, we found that the scratch adhesion strength of DLC-based and AlCrN films deposited onto Ti-6Al-4 V decreased continuously, albeit with a large data scatter, as the arithmetic mean height of the substrate profile increased (starting from a minimum value of Sa ~ 0.1 μm), irrespective of the heat treatment condition of the substrate itself [29]. The sliding wear resistance of the films, tested under unidirectional ball-on-disc configuration [22], was correspondingly improved with smoother Ti-6Al-4 V substrates. Consistently, Kolawole et al. [30], who compared the performances of DLC-based films deposited onto AISI 52100 substrates with three different finishes (Ra = 0.3, 1, and 2 μm), reported an improved scratch adhesion with the smoother finish. The reciprocating sliding wear resistance, tested against an uncoated AISI52100 ball at 200 °C, was also enhanced. The same improvement with smoother substrate finish also occurred with HiPIMS DLC films onto WC-Co, according to Khan et al. [31]. Micro-abrasive wear conditions apparently benefit from a smoother substrate as well: Martins et al. reported that the micro-abrasive wear rate of a DLC-based film onto AISI M2 steel decreased with the roughness of the substrate [32]. However, the literature results are not always univocal. For example, in the same work by Martins et al. [32], ball-on-disc sliding wear tests against an AlSi alloy counterpart (both using coated discs against AlSi balls and coated balls against an AlSi disc) did not provide univocal results as a function of the substrate finish. Salerno et al. [28] reported that DLC-coated AlSi10Mg discs suffered a lower specific wear rate and produced lower friction in a ball-on-disc test against 100Cr6 when the quadratic mean height (Sq) of the AlSi10Mg substrate was in the range of ~0.4 μm to 0.9 μm. Worse tribological performances were observed for substrate roughness values both above and below this range. Probably, differences in the nature of the DLC films themselves (e.g., their the sp^2/sp^3 ratio and H content), the interlayer architecture, and the substrate material account for the

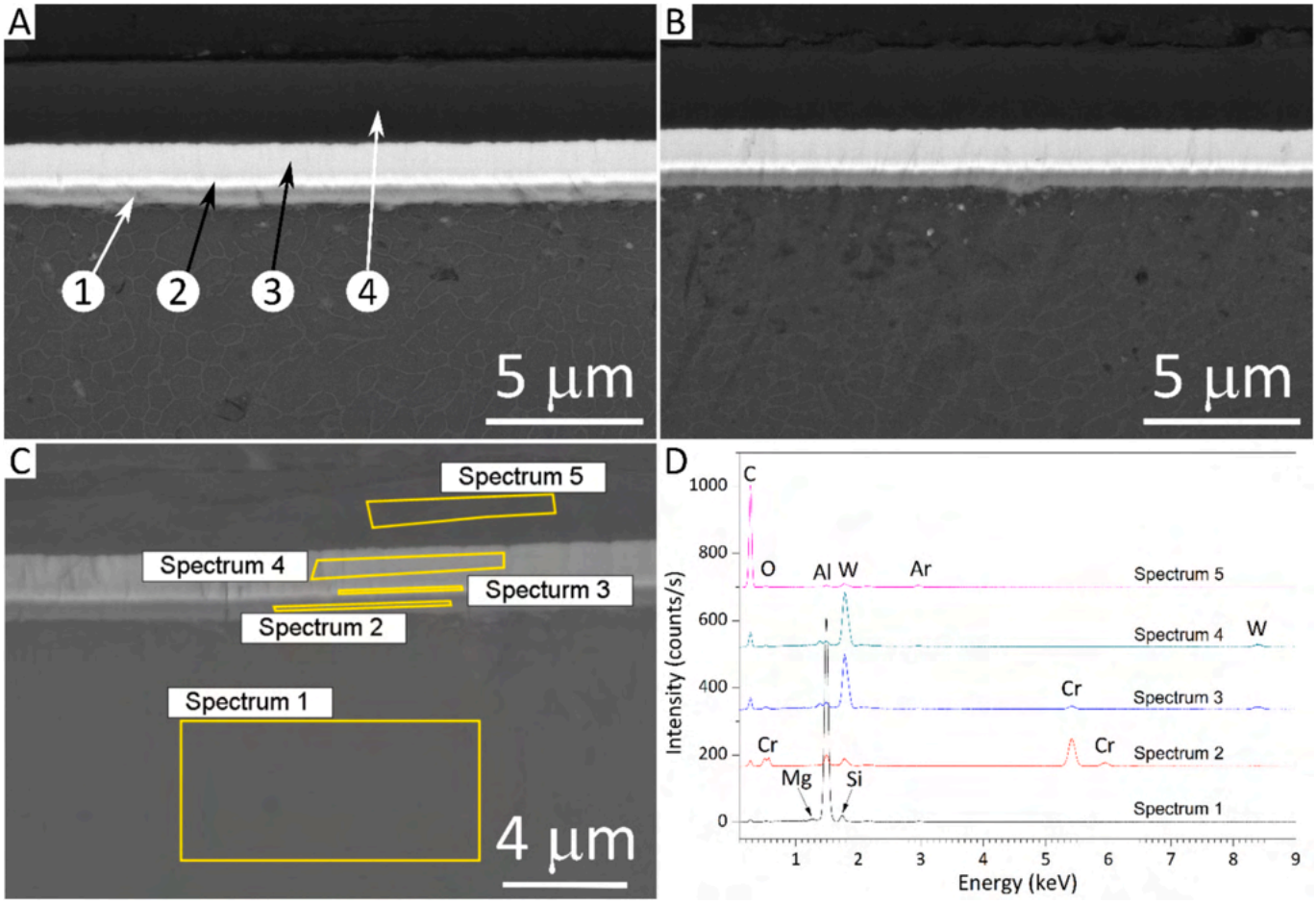

Fig. 3. Backscattered electron SEM micrographs showing the cross-sections of DLC-based films on the 7-AB-T (A) and 10-DA-B samples (B), and EDX spectra acquired on the coated 7-AB-T sample (C: acquisition areas; D: spectra). The labels in panel A indicate the four layers of the DLC-based film: 1 = Cr, 2 = bright W-C:H sub-layer, 3 = W-C:H upper sub-layer. 4 = DLC.

Table IV
Results of nanoindentation tests on coated samples.

Sample	E_{IT} ($\times 10^2$ GPa)	H_{IT} ($\times$ 10 GPa)	HV ($\times 10^3$)	HV
DLC on 7-AB-T	1.57 ± 0.31	2.2 ± 0.6	2.06 ± 0.56	2167 ± 534
DLC on 10-AB-T	1.62 ± 0.25	2.3 ± 0.6	2.17 ± 0.53	2056 ± 562
W-C:H on 7-AB-B	1.36 ± 0.15	1.3 ± 0.2	1.24 ± 0.22	1162 ± 176
W-C:H on 10-AB-B	1.35 ± 0.11	1.2 ± 0.2	1.16 ± 0.18	1235 ± 227

discrepancies existing in the literature, since all these factors would affect the contact stress distribution and the mechanical response of the systems. Notably, there seems to be some disagreement on whether the substrate roughness affects the structure of the DLC top layer itself. For example, Sheejia et al. [33] suggested that the fraction of sp^3 bonded carbon atoms, identified through Raman spectroscopy, may be slightly higher with a smoother substrate. Likewise, Kolawole et al. [30] indicated that the DLC films deposited onto smoother substrates are slightly harder than those deposited onto softer substrates. On the other hand, Martins et al. [32] and Salerno et al. [28] did not observe any change in the Raman spectrum of the DLC top layer as a function of the substrate roughness. In fact, any report of an influence of the substrate roughness on the Raman spectral features and the nanoindentation response of DLC films should probably be interpreted with care. Increased roughness can result in artefacts in both cases. A rougher surface may alter the dynamics of light scattering and consequently affect the Raman spectrum. Likewise, nanohardness measurements are reliable only when the arithmetic mean height of the indented surface (Ra) is ≤5% of the maximum penetration depth, according to the ISO 14577 standard. Nanoindentation of a very rough surface may "squeeze" elastically the asperities, resulting in an artificial increase of the measured indentation depth. In this case, hardness and elastic modulus values would be underestimated.

Despite these remaining open issues, the relation between the roughness of the substrate and the performance of the DLC-based film is not the focus of the present study, since here we aim to investigate some aspects that have been even less frequently studied.

Indeed, L-PBF techniques also result in unique as-built microstructures, often characterized by a very refined grain size and high percentage of alloying elements retained into matrix lattice due to the very rapid solidification rates of the molten pools [26]. This is certainly true for the near-eutectic Al alloys such as AlSi10Mg and AlSi7Mg. These LPBF-manufactured Al-Si-Mg alloys are generally characterized by primary equiaxed α-Al grains, disposed along the melt pool boundaries, from which other α-Al grains nucleate and growth with a columnar texture that follows the solidification heat flow [34,35]. The high solidification rates also induce, within the α-Al grains, the formation of α-Al cells surrounded by a fine network of Si-eutectic particles [36–38]. This type of microstructure confers to the as-built material very high hardness and yield strength [36–39]. These values can also be improved by direct aging heat treatments due to the ability of both as-built AlSi7Mg and AlSi10Mg to respond to precipitation hardening: the Supersaturated Solid Solution (SSS) evolves into β", β', and β-Mg_2Si

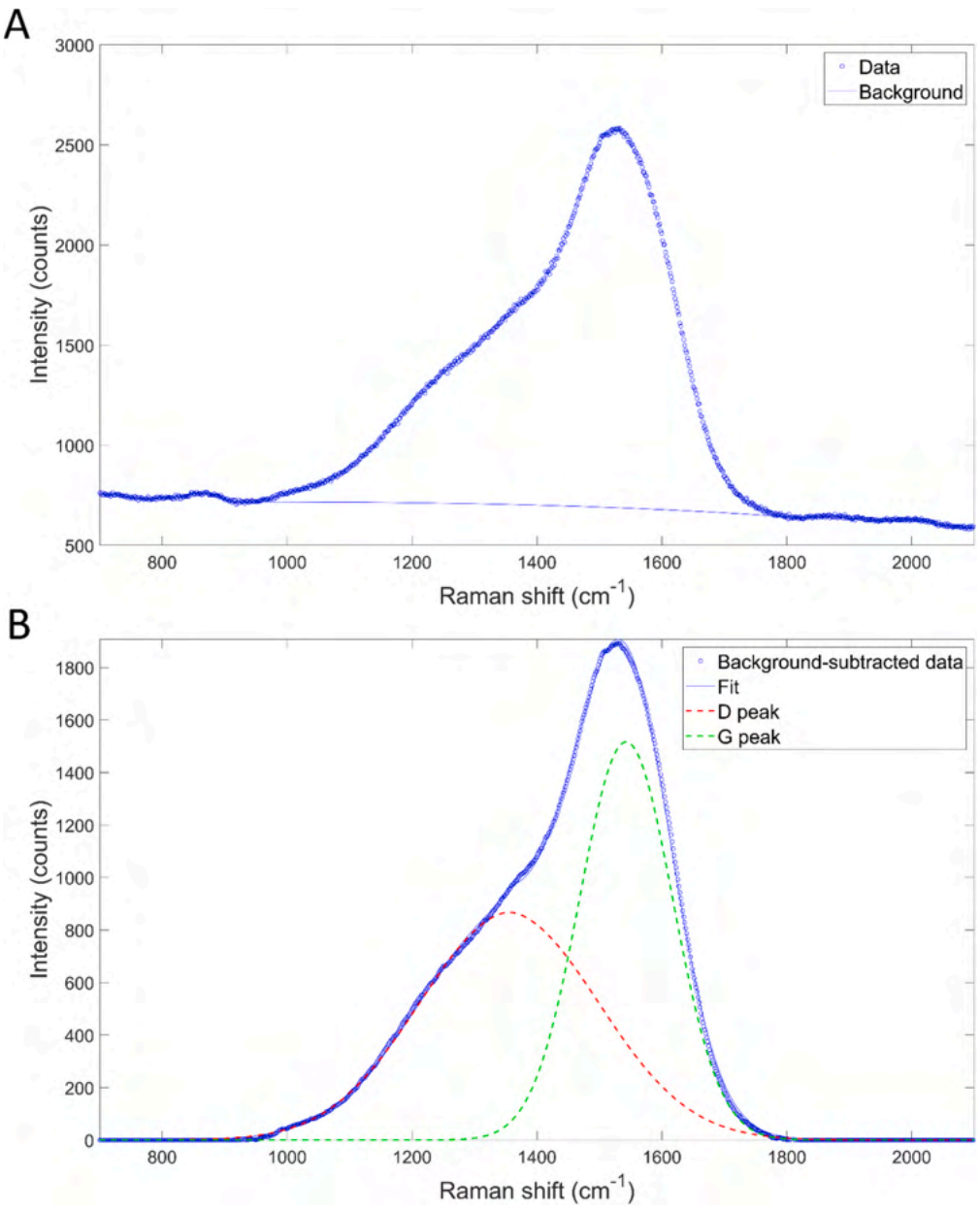

Fig. 4. Example of a Raman spectrum acquired on the DLC film on the 7-AB-B substrate, with fitted background (A), and fitting of the D and G peaks after background subtraction.

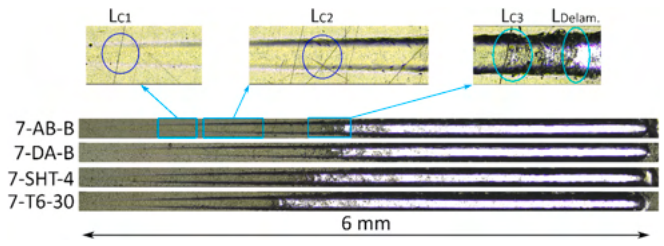

Fig. 5. Optical micrographs of representative scratch tracks on the DLC-based films deposited onto substrates in different treatment conditions, with details of the critical load morphologies.

precipitates during exposure to aging temperatures [40,41].

Conversely, for LPBF Al-alloys, a T6 heat treatment effectively acts as a softening process, resulting in lower yield strength and higher elongation to fracture compared with the as-built condition because it coarsens the networked as-built microstructure. Therefore, new types of heat treatments can be considered, and they have indeed been frequently explored in the literature [39]. As previously mentioned, one possibility is to perform in-situ or post-processing direct aging heat treatments ($T < 200\ ^{\circ}C$) that result in improved strength and a slight loss of ductility compared to the as-built samples if they were manufactured on a build platform at room temperature [36,39].

The high yield strength (hence, also high hardness) of as-built or direct-aged LPBF Al—Si alloys can be exploited to improve the mechanical support offered to DLC-based films. Thus, provided that the limited elongation to fracture of these alloys is acceptable for the intended application, it could be advantageous to coat as-built or directly aged LPBF-manufactured parts. There is a chance that these types of substrates offer sufficient mechanical support without the need for costly interlayers.

The situation is complicated by the fact that, even though the

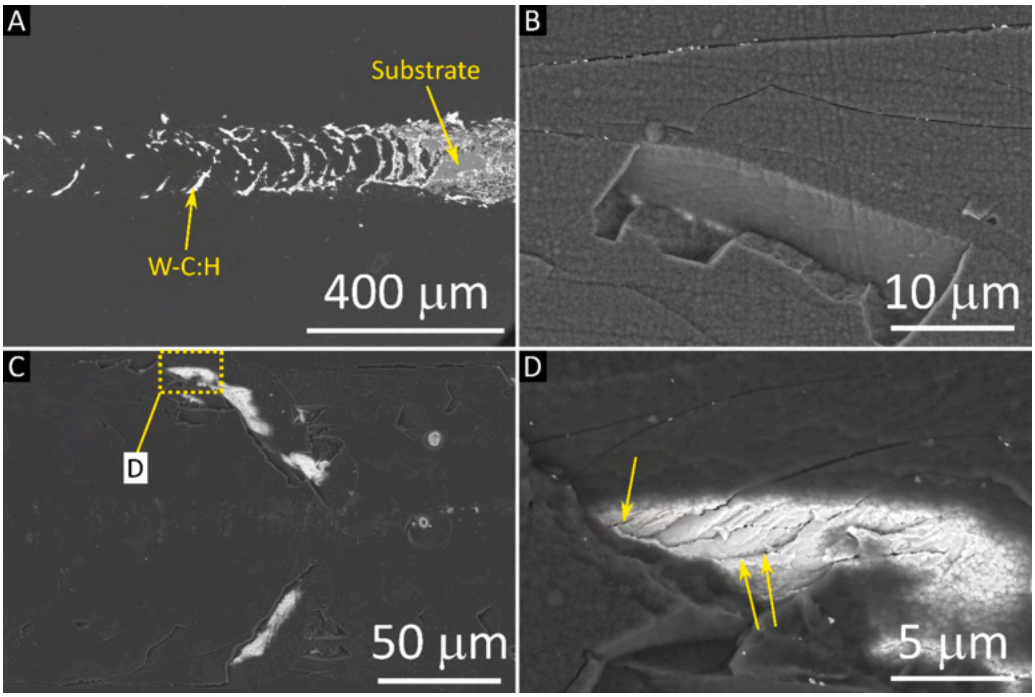

Fig. 6. SEM micrographs of one of the scratch tracks on the DLC-coated 10-AB-T sample. A: overview of the region around the $L_{Delam.}$ critical load; B: detail of a chipping event in the DLC top layer; C: extended chipping event affecting both the DLC top layer and the W-C:H intermediate layer; D: detail of the area marked in panel C. The arrows indicate cracks existing in the W-C:H intermediate layer but not extending to the DLC top layer.

Table V
Critical loads identified in the scratch adhesion tests on the DLC-based and the W-C:H terminated films on as-built AlSi10Mg and AlSi7Mg substrates.

Sample	L_{C1} [N]	L_{C2} [N]	L_{C3} [N]	$L_{Delam.}$ [N]
DLC-based film on 10-AB-T	3.5 ± 0.2	8.3 ± 0.3	13.9 ± 0.9	15.7 ± 0.5
DLC-based film on 10-AB-B	3.2 ± 0.1	8.2 ± 0.4	16.1 ± 2.2	17.1 ± 2.1
W-C:H film on 10-AB-B	2.9 ± 0.3	8.0 ± 1.1	9.2 ± 1.2	10.4 ± 0.7
DLC-based film on 7-AB-T	2.9 ± 0.1	6.8 ± 0.5	13.1 ± 0.1	14.1 ± 0.5
DLC-based film on 7-AB-B	3.0 ± 0.1	7.6 ± 0.4	12.6 ± 0.5	14.1 ± 0.5
W-C:H film on 7-AB-B	2.8 ± 0.3	7.3 ± 0.6	9.7 ± 0.3	11.2 ± 0.4

deposition of DLC by PA-CVD processes can be performed at relatively low temperatures of 160–180 °C, these temperatures are, in fact, in the range of the aging temperatures of Al alloys [36,39]. Thus, an as-built or solutionized substrate could arguably be effectively aged during the deposition process itself [42], whereas an aged substrate could experience over-aging. Lugscheider et al. [43], for example, showed that the hardness of an Al-alloy substrate could be substantially degraded if the temperature during a PVD coating process was allowed to increase too much.

It is therefore necessary to clarify the interplay between the heat treatment condition of L-PBF Al-alloy substrates, like AlSi10Mg and AlSi7Mg, and the performance of DLC-coated systems. In this work, DLC-based films were deposited by a combined PVD and PA-CVD process onto AlSi10Mg and AlSi7Mg alloys in four different conditions: as-built, directly aged, solution-treated and T6 (solutionized and aged). After a microstructural and mechanical characterization of the substrates in the different conditions and the films, the adhesion and the tribological performance of the coated systems were assessed by scratch tests and ball-on-disc dry sliding wear tests, respectively. The resulting failure mechanisms were investigated by scanning electron microscopy inspection of worn samples and by Raman spectroscopy analysis of the wear debris.

2. Experimental

2.1. Substrates and DLC-based coating deposition

Gas-atomized Al-Si-Mg powder particles, whose chemical composition is listed in Table I, were used to manufacture the AlSi7Mg and AlSi10Mg substrates. Both powders, manufactured by Tekna®, had diameters ranging from 20 to 63 µm. When both AlSi7Mg (labelled as "7-") and AlSi10Mg (labelled as "10-") will be characterized by similar results, the "Al-Si-Mg" label will be used to refer to them collectively.

The LPBF process was conducted with an SLM®280 machine where two IPG fibre lasers melted 90 µm-thick powder layers with a power of 370 W, a scanning speed of 1400 mm/s, and a hatch spacing of 70 µm. Bars of 10x10x300 mm^3 size were manufactured on a build platform heated to 150 °C. The substrates used to deposit the DLC-based thin film were cut from both the farthest (labelled as "top") and nearest (labelled as "bottom") zones from the heated build platform. The as-built top and bottom substrates will be labelled with the suffixes "-T" and "-B", respectively.

Each Al-Si-Mg substrate was first mechanically ground with SiC papers and then polished with colloidal silica suspension for both the microstructural investigation and coating deposition process. In fact, as explained in the Introduction, the effect of substrate roughness on the performance of the DLC-based films was not the focus of this study. Therefore, we rather sought to avoid roughness as a confounding factor [28]. The Sa values of the polished substrates, which were measured with a non-contact 3D profilometer (Taylor Hobson, Leicester, United Kingdom), were of 0.07 ± 0.01 µm. Even though, as discussed in the Introduction and in [28], such an extremely smooth surface finish may not maximize the performance of DLC-based films deposited onto Al-Si-Mg alloy substrates, achieving a reproducible finish on all substrates allowed to avoid any influence from roughness itself. Moreover, a very smooth surface means that local stress concentrations at roughness asperities were minimized. Therefore, the mechanical response of the system reflected more clearly the macro-scale stress distribution between the harder, stiffer film and the substrate. Thus, this was the most

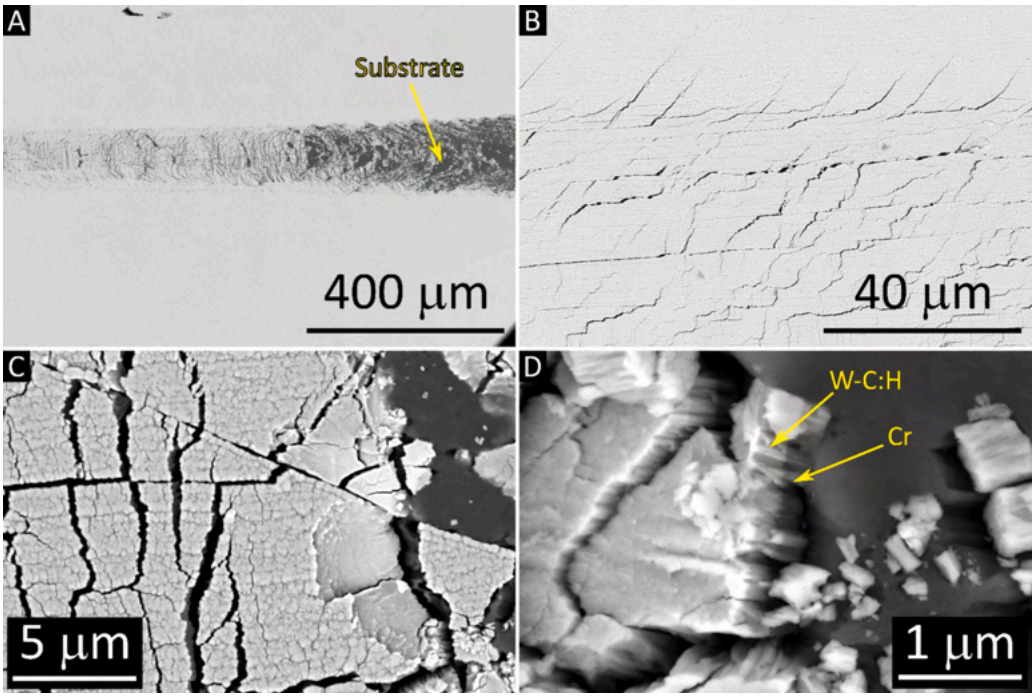

Fig. 7. SEM micrographs of one of the scratch tracks on the 10-AB-B sample with the W-C:H coating. A: overview of the region around the $L_{Delam.}$ critical load; B: detail of the extensive microcracking of the W-C:H layer; C: cracks of increasingly large width expose the AlSi10Mg substrate; D: detail of the cracked film where the two layers are visible on the fracture.

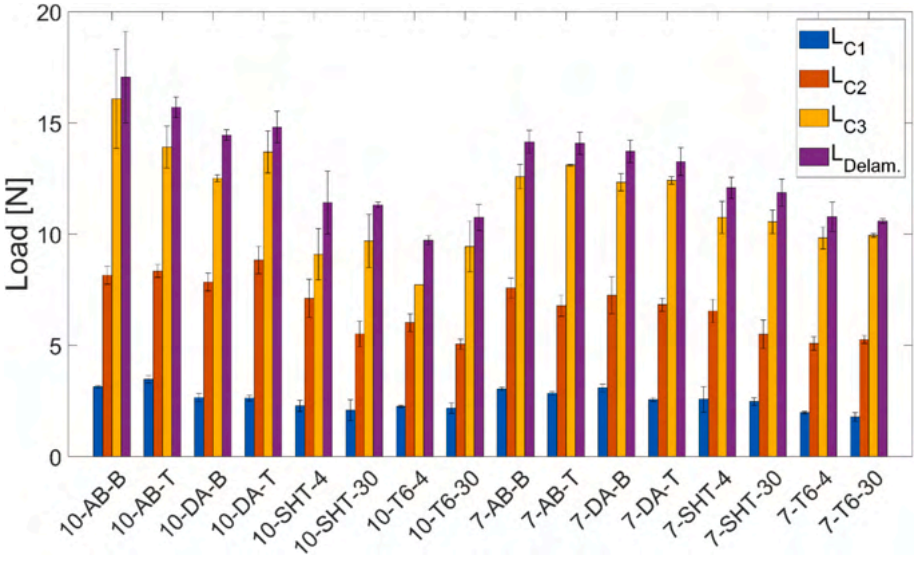

Fig. 8. Critical loads measured for the DLC-based films on all types of substrates.

suitable experimental condition to highlight the effects of changing the mechanical properties of the Al-Si-Mg alloy substrates through different heat treatments.

To evaluate the influence of the hardness of Al-Si-Mg and its ability to respond to aging phenomena during the DLC deposition process, the substrates were treated in different conditions as listed in Table II. These heat-treatment conditions, which represent the peak-aging, were chosen in relation to the results previously presented and discussed in [44]. Each heat treatment was conducted in a muffle furnace (Nabertherm GmbH, Lilienthal, Germany), with temperatures controlled with a K-type thermocouple. To indicate the different substrate conditions, the labels "AB", "DA", "SHT", and "T6" will hereafter designate the as-built, direct-aged, solution heat-treated, and artificially-aged substrates, respectively. Thus, for example, the direct aged top and bottom substrates are labelled as "DA-T" and "DA-B", respectively. Lastly, the "-30" and "-4" suffixes of the SHT samples indicate 30 min and 4 h soaking time at 500 °C, respectively.

The DLC-based film deposited on all substrates consisted of a multilayer architecture, namely Cr + W-C:H + DLC (a-C:H type). This means that adhesion was made with a chromium layer, followed by a W-C:H support layer and the top functional a-C:H layer.

A Hauzer Techno Coating HTC1200 coating unit was used for the deposition of the DLC-based film for this work. After an etching step performed using an Ar plasma generated by a filament source operated at 180 A with a 100 sccm Ar flow and a pulsed substrate bias of – 150 V, the adhesion and the support layers were deposited by unbalanced

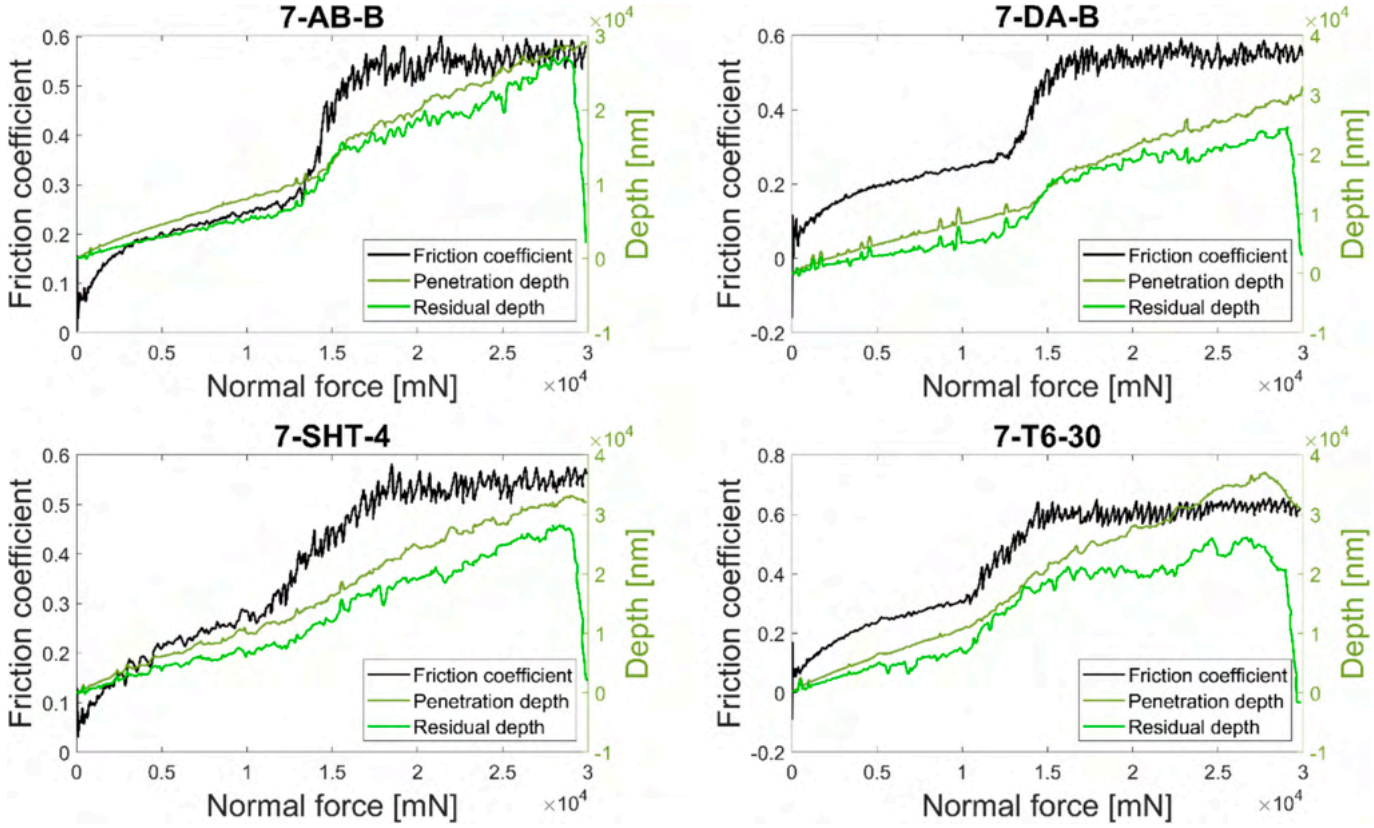

Fig. 9. Instrumental recordings of friction coefficient, total penetration depth of the indenter during the test, and residual track depth after the test, plotted as a function of the applied normal load for the scratch tracks shown in Fig. 5.

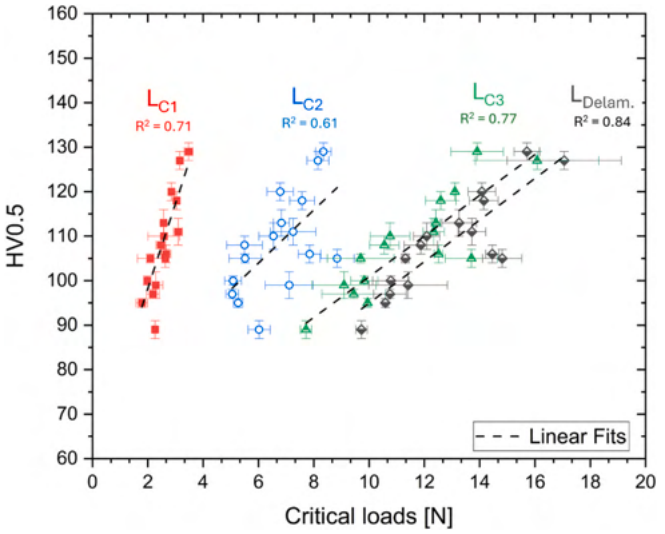

Fig. 10. Correlation between the critical loads and the hardness of the coated substrate.

magnetron sputtering (UBM).

For this purpose, the coating unit was equipped with two Cr 99.9 wt % and two WC (Co-free) targets, all of 170 × 1000 mm size. For the deposition of the Cr adhesion layer, the Cr targets were run in pure Argon plasma at 6 kW power each, with an Ar flow rate of 300 sccm and a deposition time of 20 min. For the W-C:H intermediate layer, the WC targets were operated with an Ar + C_2H_2 mixture, at 5.5 kW power each. The Ar and C_2H_2 flow rates were 300 sccm and 500 sccm, respectively, and the deposition time was 120 min. The deposition of both the adhesion and the intermediate layer was run in self-bias mode, i.e., no external bias voltage was applied to the substrates. The a-C:H top layer was deposited in a pure C_2H_2 plasma (500 sccm C_2H_2 flow rate). The plasma was generated by applying a pulsed bias of −740 V, in voltage control mode, at a frequency of approximately 40 kHz. The deposition time was 130 min. In all cases, the deposition pressure was temperature- and loading-dependent, as the process was flow-controlled. Anyhow, for the a-C:H step, the pressure value, monitored through a Baratron, was in the range of 5×10^{-3} to 8×10^{-3} mbar.

Additionally, a deposition run performed only with the as-built substrates was interrupted after the W-C:H intermediate layer. This enabled the measurement of the micromechanical properties and the adhesion strength of the W-C:H layer itself.

The temperature during the deposition process was controlled with four thermocouples installed inside the coating unit. Two static thermocouples were mounted on the chamber wall, close to the heating elements, while two rotating thermocouples were mounted directly on the planetary holder where the parts to be coated were fixed. The static thermocouples were employed to monitor the heaters temperature, while the rotating ones governed the process and their temperature signals were fed into a PID controller that acted on the heating elements power to reach and stabilize the temperature around the setpoint, in this specific case 175 °C. As a result, the applied heating power was around 20 kW. The system was heated before the etching and deposition steps; subsequently, no heating power was employed during the etching and coating steps, since the exposure to the plasma and the powered targets was sufficient to keep a quite stable temperature around the previously attained setpoint value.

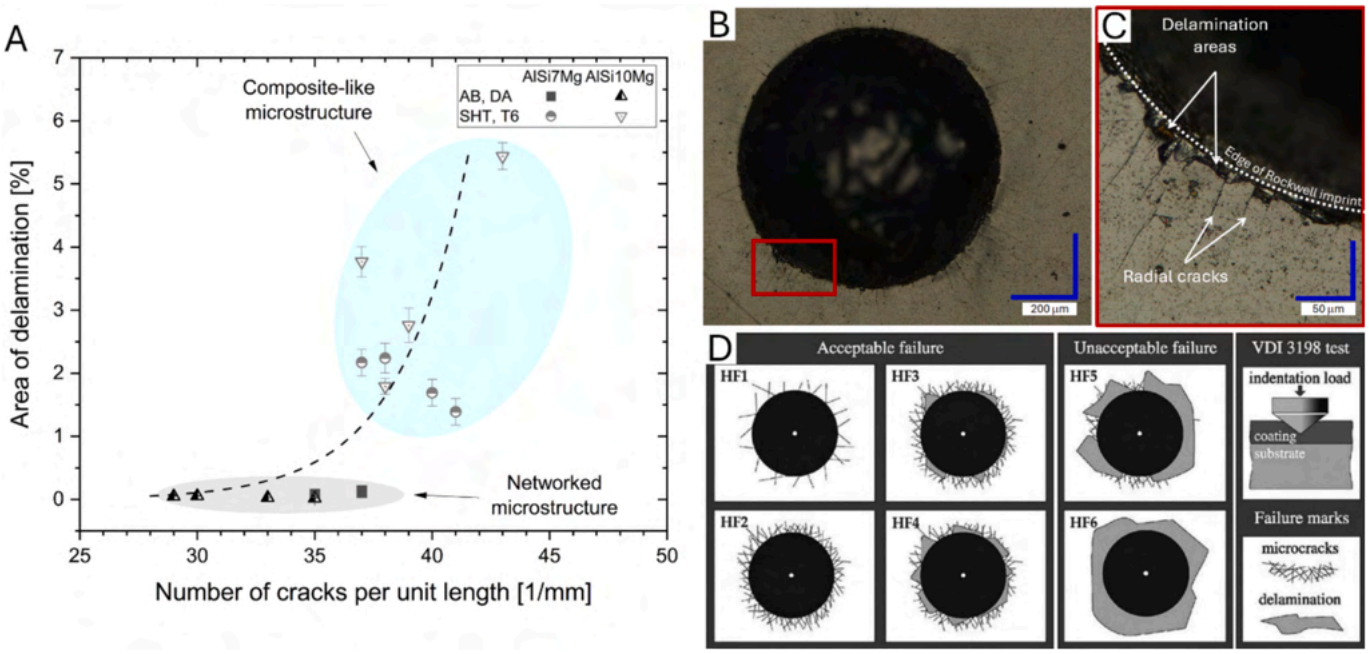

Fig. 11. correlation between the area of delamination and the number of cracks per unit length (A) in the Rockwell indentation test. The optical micrographs show the entire Rockwell imprint (B) and a portion of the same imprint (C). Panel (D) depicts the failure chart of the VDI 3198 indentation test (reprinted from reference [22]).

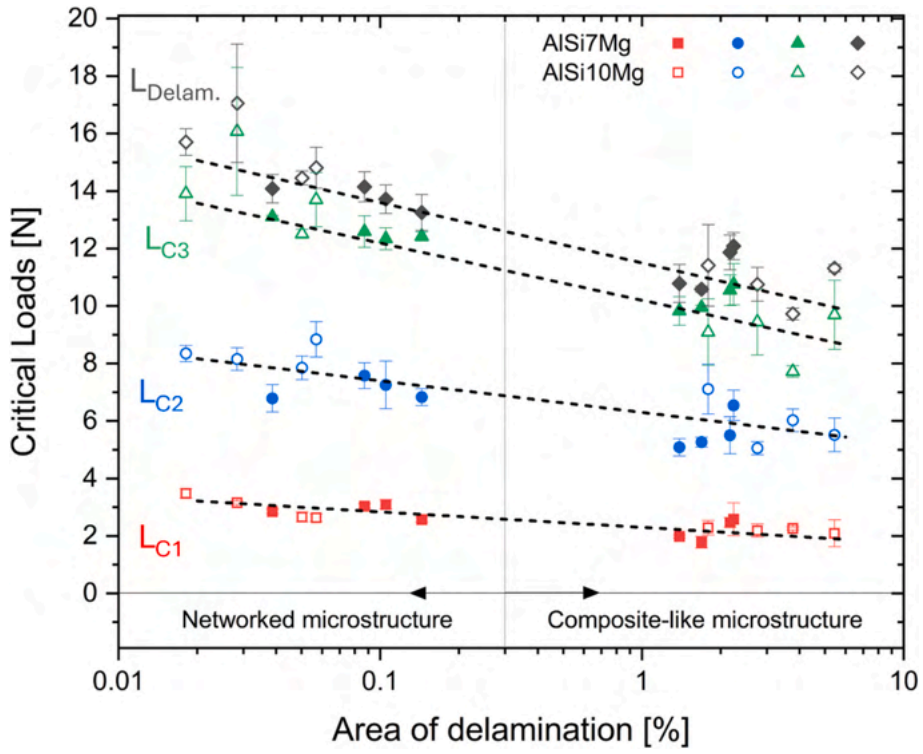

Fig. 12. Correlation between the critical loads in the scratch test and the area of delamination obtained from the Rockwell VDI tests performed on coated Al-Si-Mg substrates.

2.2. Microstructural and micromechanical characterization of bare and coated substrates

The microstructure of as-built and heat-treated bare substrates was analysed by optical microscopy (OM, DMi8 Leica, Wetzlar, Germany) and scanning electron microscopy (SEM, Auriga compact FIB-SEM, Zeiss, Oberkochen, Germany) equipped with an EDS detector (Ultim® Extreme, Oxford Instruments, Abingdon, Oxfordshire, England).

The Vickers microhardness HV of the substrates was measured before and after the coating deposition process by using load of 500 gf and dwell time of 15 s, according to the ISO 6507 standard. In the latter case, Vickers measurements were performed after coating removal with SiC

Table VI
Specific wear rates and average friction coefficients measured during the two replicates of the ball-on-disc sliding wear tests on each sample[1]. Where the coating delaminated before the end of the test, no results are given but the sliding distance at which the delamination occurred is noted.

Sample	1st replicate		2nd replicate	
	Sample wear rate [$\times 10^{-7}$ mm^3/(N•m)]	Friction coefficient	Sample wear rate [$\times 10^{-7}$ mm^3/(N•m)]	Friction coefficient
7-AB-B	9.2 ± 1.6	0.13 ± 0.01	6.3 ± 0.7	0.13 ± 0.01
7-AB-T	5.3 ± 0.6	0.12 ± 0.01	5.7 ± 0.7	0.13 ± 0.01
7-DA-B	7.6 ± 2.5	0.13 ± 0.01	Delaminated (~ 600 m)	
7-DA-T	7.4 ± 1.9	0.12 ± 0.01	5.3 ± 0.6	0.13 ± 0.01
7-SHT-4	10.8 ± 2.5	0.13 ± 0.01	11.8 ± 4.0	0.13 ± 0.01
7-SHT-30	12.1 ± 1.0	0.14 ± 0.01	Delaminated (~ 480 m)	
7-T6–4	Delaminated (~ 740 m)		Delaminated (~ 380 m)	
7-T6–30	Delaminated (~ 780 m)		Delaminated (~ 500 m)	
10-AB-B	6.8 ± 2.5	0.13 ± 0.01	4.7 ± 0.7*	0.09 ± 0.01
10-AB-T	3.6 ± 0.3	0.12 ± 0.01	10.3 ± 2.3	0.13 ± 0.01
10-DA-B	35.2 ± 26.8*	0.13 ± 0.01	16.6 ± 8.1	0.14 ± 0.01
10-DA-T	5.7 ± 0.5	0.13 ± 0.01	Delaminated (~ 600 m)	
10-SHT-4	8.8 ± 1.2	0.13 ± 0.01	Delaminated (~ 200 m)	
10-SHT-30	5.3 ± 0.7	0.14 ± 0.01	Delaminated (~ 320 m)	
10-T6–4	Delaminated (~ 340 m)		Delaminated (~ 120 m)	
10-T6–30	Delaminated (~ 260 m)		Delaminated (~ 360 m)	

* Specific wear rate averaged over 3 profile measurements (4th profile returned much higher value).
[1] The error associated with the sample wear rate was obtained by propagating the error among the 4 profile measurements done on each wear track; the error on the ball wear rate was propagated from the error on the wear scar diameter measurement.

papers. The associated error was calculated as the standard deviation of nine indentations.

The microstructure of the coatings was examined on polished and slightly etched cross-sections. The samples were sectioned with a resin-bonded Al_2O_3 disc, cold-mounted in a two-component epoxy resin, ground with diamond-based discs of P600 and P1200 grit size, and polished using first a metal-backed pad spread with a 3 μm-size poly-crystalline diamond suspension. Final polishing was performed with a colloidal silica suspension (oxide polishing suspension, OPS) of 60 nm average size on a nonwoven cloth. The polished specimens were etched with Keller's reagent for ~10–15 s, ultrasonically cleaned in iso-propanol, and sputter-coated with a ~10 nm-thick Au layer for scanning electron microscope (SEM) observation. A Nova NanoSEM 450 system (Thermo Fisher Scientific, Eindhoven, NL), equipped with an energy-dispersive X-ray (EDX) microanalysis system (Quantax 200 with an XFlash 6|10 detector – Bruker Nano GmbH, Berlin, DE) was used for the investigations.

Micro-Raman spectra of the DLC top layer were acquired using a Nd:YAG laser source with a wavelength of 532 nm. The laser power was filtered to 3.2 mW to prevent thermal alteration and focused through a 100× objective; the resulting signal was analysed with a 600 g/mm diffraction grating and a CCD detector. Spectra were obtained by averaging 20 accumulations of 6 s duration.

The hardness of the DLC-based films was measured on their top surface using a Berkovich nanoindenter (NHT^3, Anton Paar TriTec, Corcelles – CH) at a maximum load of 10 mN (20 mN/min loading and unloading rate; 15 s hold at maximum load), which corresponded to a maximum penetration depth around 195 nm and a contact depth of around 130 nm. The measurements were performed and analysed according to the ISO 14577 standard, using an indenter calibrated and periodically verified against a fused silica reference. A total of 120 indents were performed.

Because the DLC-based film was the same on all substrates and its growth was reasonably not influenced by the heat treatment condition of the underlying surface (all samples having been finished to the same roughness), the cross-section microstructural characterization was presented only for one type of substrate (as-built AlSi7Mg) and, likewise, hardness was measured only for the films on the as-built AlSi7Mg and AlSi10Mg substrates, and Raman spectra were only acquired from the surface of the 7-AB-B sample. Using the harder as-built surfaces for nanoindentation ensured that the influence from the substrate was minimized.

Additional nanoindentation tests were performed on the as-built samples coated with the W-C:H layer (without DLC top layer).

2.3. Adhesion testing of the coated systems

The adhesion of the DLC-based films in all combinations of substrate material, build position, and heat treatment condition, as well as that of the W-C:H film on the as-built substrates, was studied by scratch testing (Micro-Combi Tester, Anton Paar TriTec), using a conical diamond indenter with a 100 μm tip radius and operating over a load range of 0.02–30 N with a 6 mm scratch length and a 6 mm/min speed. Consistent with the ISO 20502 standard, the critical loads for the onset of damage in the films were determined by optical microscopy, operating at 200× magnification. The critical loads identified in this work were the load for crack formation (L_{C1}), chipping of the coating along the track sides (L_{C2}), chipping of the coating across the entire track width (L_{C3}), and continuous delamination of the coating ($L_{Delam.}$). The tangential force on the sample was recorded via a load cell attached to the sample holder; hence, the friction coefficient was computed as the ratio of the tangential force over the applied normal load, controlled through a feedback actuation system with a load cell attached to the indenter tip. By recording the position of the tip with an LVDT sensor, and by performing pre- and post-scans over the tested area with a low load of 0.02 N, the penetration depth of the indenter during the test (difference between the position of the indenter during the test and the initial profile) and the residual depth (difference between the final and initial profile) were also recorded. These instrumental recordings were employed to assist in the identification of the critical loads. The scratch tracks on the DLC- and W-C:H coated AlSi10Mg substrates in as-built conditions were also observed by SEM (Nova NanoSEM 450).

In addition, the coating/substrate adhesion was also evaluated through Rockwell VDI test according to VDI 3198 standard [45] by applying a statistical analysis of the cracks and delaminations formed during the indentations, as discussed in [22]. Each indentation was carried out at room temperature by using ZHR Rockwell hardness tester (Zwick/Roell, Ulm, Germany) with a load of 60 kgf and a conical diamond indenter.

2.4. Dry sliding wear testing of the coated systems

The dry sliding wear behaviour of all samples was studied by unidirectional rotating ball-on-disc testing (THT, Anton Paar TriTec), using

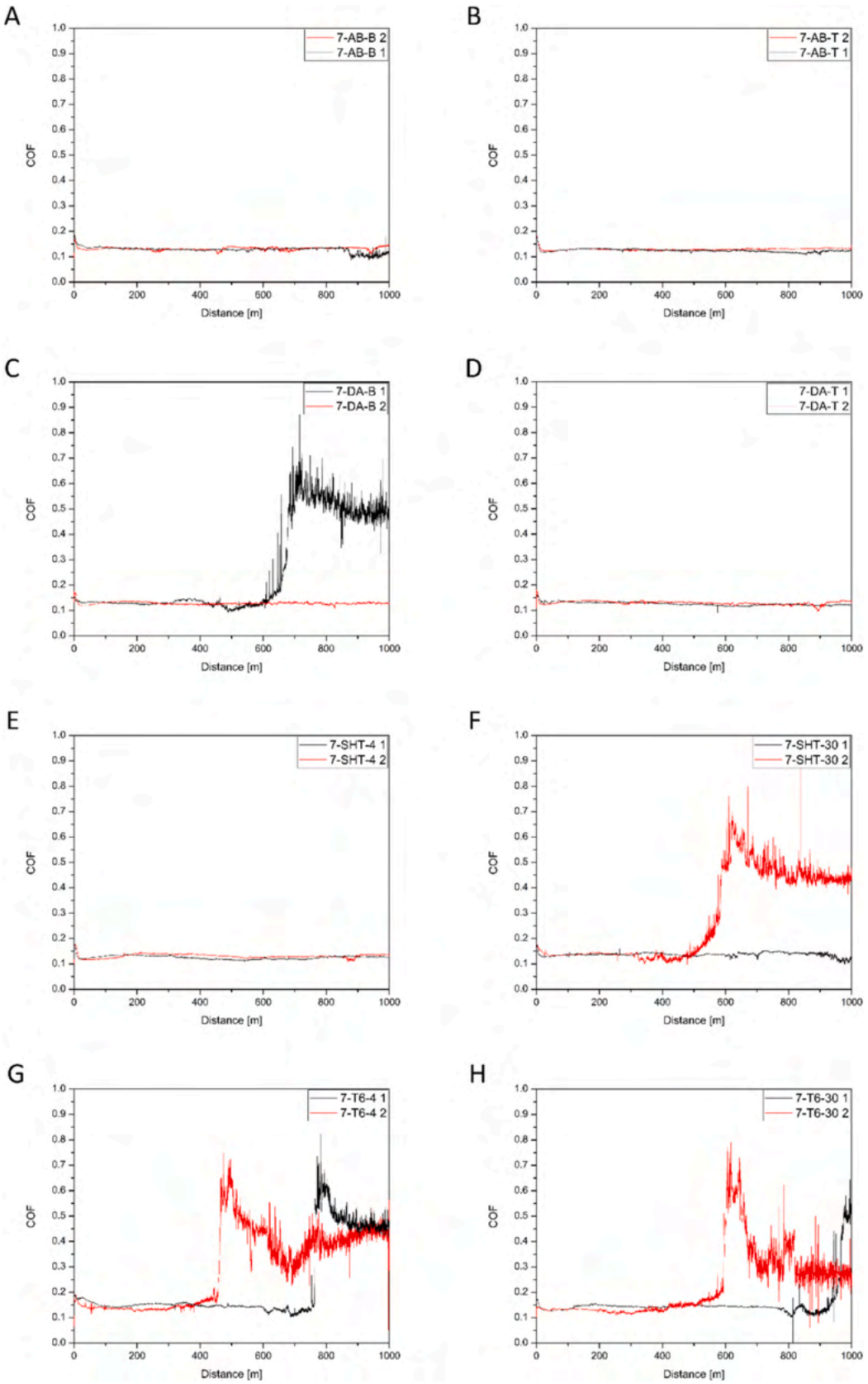

Fig. 13. Friction curves measured during the two replicates of the wear tests on the DLC-coated samples 7-AB-B (A), 7-AB-T (B), 7-DA-B (C), 7-DA-T (D), 7-SHT-4 (E), 7-SHT-30 (F), 7-T6–4 (G), and 7-T6–30 (H).

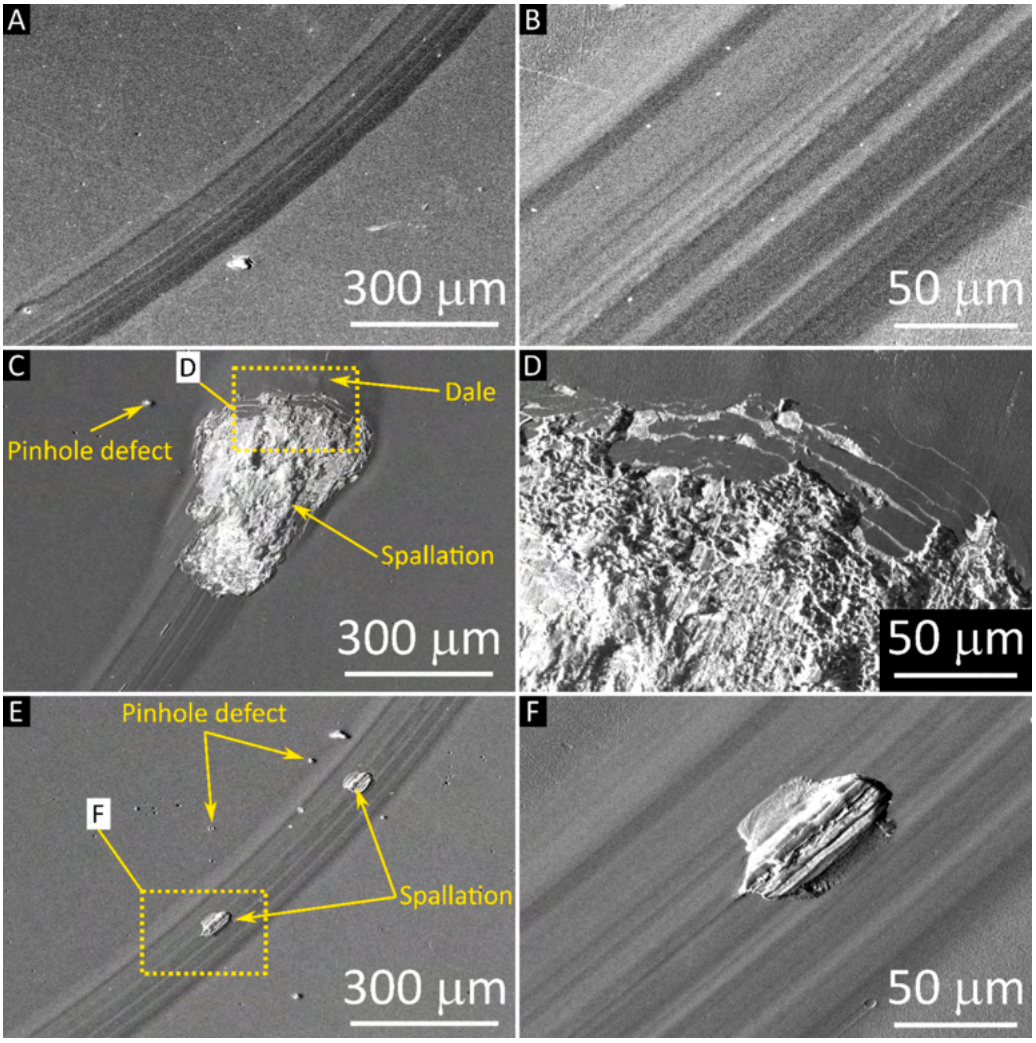

Fig. 14. SEM micrographs showing the worn surface of the DLC-based film on the 7-AB-B sample at three different locations (A-B, C—D, E-F) – overviews (A, C, E) and details (B, D, F).

an Al_2O_3 ball with 3 mm diameter as counterpart. Al_2O_3 is a chemically inert material that does not introduce additional tribochemical phenomena that would complicate the analysis of wear mechanisms, and the choice of a 3 mm-diameter ball was meant to produce a quite high contact pressure to probe the response of the systems under demanding conditions. The normal load was 5 N: assuming E = 70 GPa, $\nu = 0.33$ for both AlSi10Mg and AlSi7Mg, and E = 370 GPa, $\nu = 0.23$ for the Al_2O_3 ball, the average contact pressure on an uncoated substrate would be ~815 MPa and the maximum shear stress would be ~380 MPa at a depth of ~21 µm. This confirms that, even with the DLC-based film, the maximum shear stress was located in the substrate, and it was high enough to approach or exceed its yield strength. The wear track diameter was 7 mm, the linear speed was 0.20 m/s and the total sliding distance was 1000 m. The sample and the ball were cleaned with isopropanol before and after each test. Two repeats were done for each sample type.

The wear volume loss of the samples was measured by optical profilometry (ConfoSurf profilometer, Confovis GmbH, Jena – DE, connected to a Nikon Eclipse LV150N optical microscope) using a structured illumination method. Profiles were acquired along four stripes of 200 µm length located at 90° from each other around the circular wear track, operating with a 50× objective. The average cross-sectional area of the track was thus obtained and multiplied by the length of the circular track to determine its volume. The results were converted to specific volumetric wear rates in units of $mm^3/(N \bullet m)$ and expressed as average ± half-difference.

The worn surfaces of the coated samples and selected cross-sections, prepared as described in Section 2.2, were observed by SEM (Nova NanoSEM 450). The worn surfaces of the balls were observed by optical microscopy (Olympus GS10), and micro-Raman spectra were acquired on the transfer material visible on the wear track on the ball. Spectra were acquired in the same conditions as described in Section 2.2, averaging 6 accumulations of 20 s duration each.

3. Results and discussion

3.1. Microstructure and hardness of the substrates

Fig. 1 A shows a representative AB microstructure of both bottom and top LPBF-manufactured Al-Si-Mg bare substrates that were formed by α-Al cells decorated with Si-eutectic particles arranged into a network structure. The SEM micrograph also revealed the presence of rod- and circle-shaped Si-nanoparticles into α-Al cells (yellow arrows in Fig. 1 A). Nevertheless, the exposure to the build platform heated to 150 °C resulted in some microstructural differences between the substrates taken from the portions of the bars that were the closest (AB-B) or the farthest (AB-T) from the build platform. Indeed, the cell-like structure of the AB-B substrates showed a more equiaxed morphology, attributed to

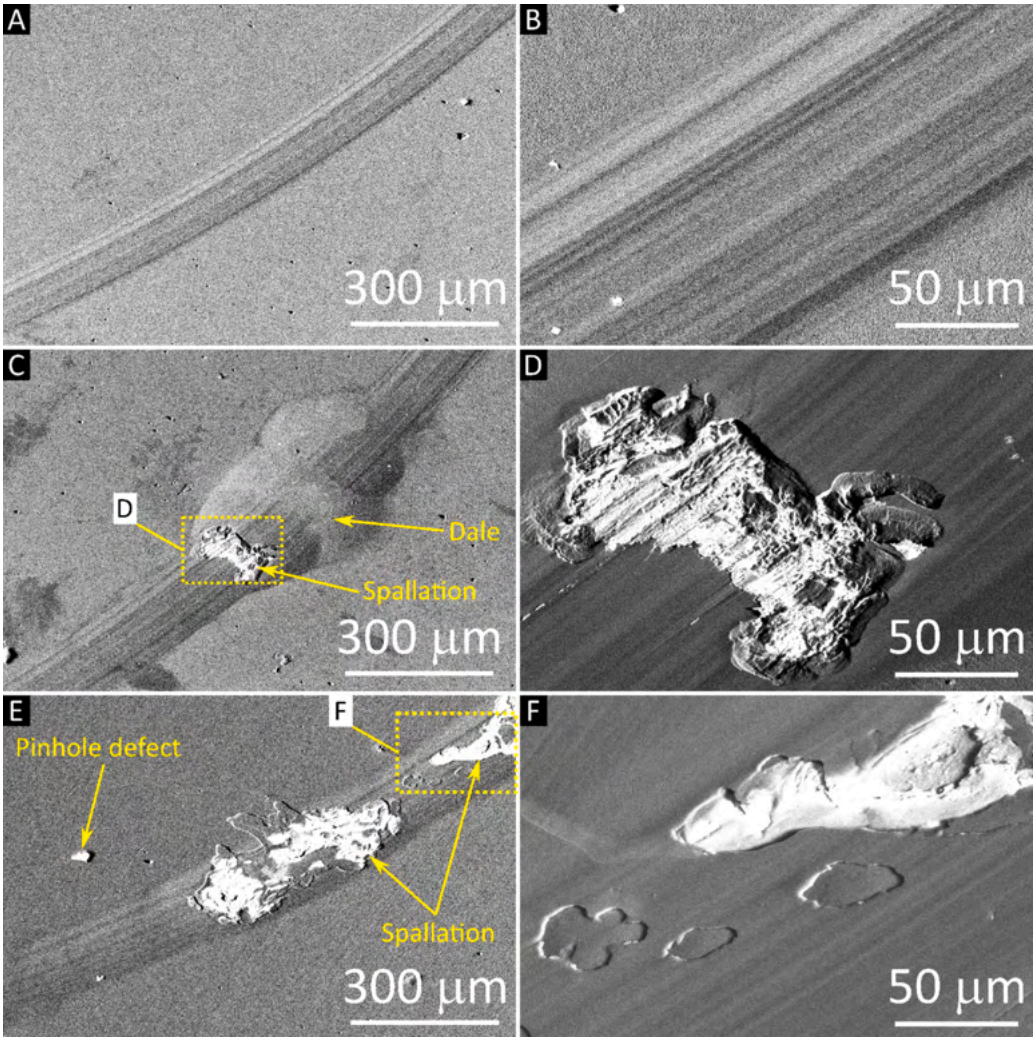

Fig. 15. SEM micrographs showing the worn surface of the DLC-based film on the 10-AB-T sample at two different locations (A-B, C—D) and the 10-AB-B sample (E-F) – overviews (A, C, E) and details (B, D, F).

the presence of sub-grain structures in the α-Al cells, as well as a higher amount of Mg_2Si, β", and β' precipitates, compared to the AB-T substrates. These findings were confirmed by TEM observations performed in [44] on the same bare AB substrates.

As a result of these microstructural differences, Fig. 2, which lists the hardness of all the AlSi7Mg and AlSi10Mg substrates before and after the deposition of the DLC-based film, shows that the bare AB-T substrates (prior to the deposition process) always exhibited lower HV values than the AB-B ones. The exposure to the direct aging temperature of 175 °C for 8 h did not alter the networked microstructure in term of its morphology and size. In fact, the dimensions of the α-Al cells and the thickness of the Si-eutectic network remained unchanged before and after the exposure to aging temperature (Table III).

However, there was a measurable change in hardness of the substrates both after the direct aging treatment, and after the deposition of the DLC-based film, which also involved prolonged exposure to the same temperature of 175 °C. Accordingly, in most cases the AB substrates after deposition and the DA substrates before deposition exhibited very similar hardness (Fig. 2). The high amount of SSS in the AB-T bare substrates promoted precipitation phenomena during the exposure to the deposition or the direct aging temperature that resulted in an increase in HV: after deposition, the hardness increased from (111 ± 3) $HV_{0.5}$ and (128 ± 3) $HV_{0.5}$ to (128 ± 4) $HV_{0.5}$ and (132 ± 4) $HV_{0.5}$ for the 7-AB-T and the 10-AB-T samples, respectively. The exposure of the AB-B bare samples to the deposition or direct aging temperature, on the contrary, reduced the HV values due to the coarsening of the precipitates previously formed during the LPBF process, despite the lack of changes to the Si-eutectic network. These effects cannot be seen by optical micrographs, but they were revealed through TEM observations in [44] after the exposure of AB-T samples to 175 °C.

When the DA substrates were exposed to the deposition temperature, the precipitation sequence continued to progress from semi-coherent to in-coherent precipitates; therefore, both the peak-aged DA-T and DA-B bare substrates showed a reduction in HV values after the deposition process (Fig. 2). No other microstructural variations that might have influenced hardness occurred during the deposition of the DLC-based film (as previously affirmed and as will be possible to observe in the cross-section shown in Fig. 18).

The exposure to the SHT temperature of 505 °C, by contrast, transformed the networked microstructure into a composite-like structure (Fig. 1B,C) where globularized Si-particles were embedded within an α-Al matrix. The destruction of the Si-eutectic network and the coarsening of the α-Al grains during the solution heat treatment significantly reduced the HV values of both 7-AB and 10-AB substrates (Fig. 2). Increasing the soaking time from 0.5 h (Fig. 1B) to 4 h (Fig. 1C) coarsened the globularized Si-particles, increasing their equivalent diameter from approximately 1.2 µm to 3.5 µm, and rendered their distribution in the Al matrix more uniform due to diffusion-controlled phenomena

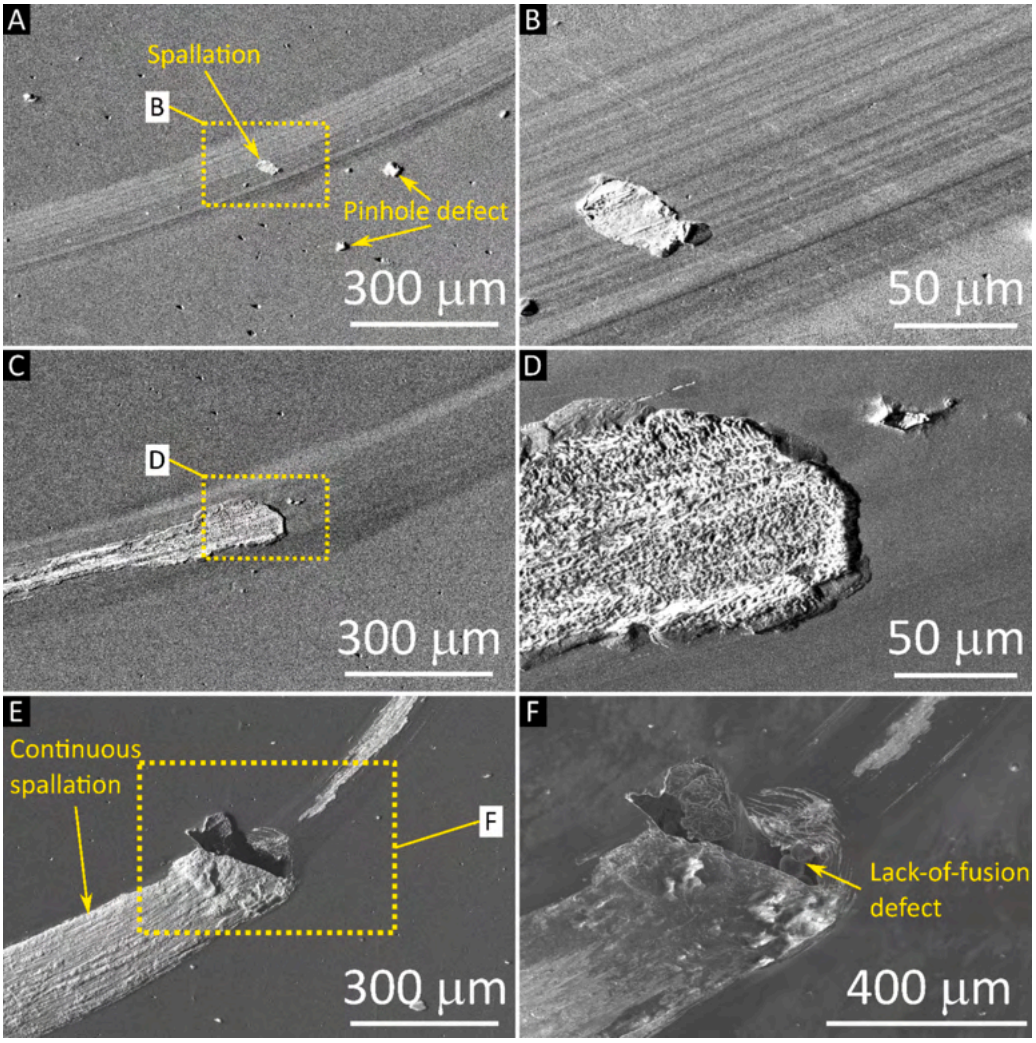

Fig. 16. SEM micrographs showing the worn surface of the DLC-based film on the 10-DA-T sample A-B) and the 10-DA-B sample at two different locations (C—D, E-F) – overviews (A, C) and details (B, D).

[46]. The same diffusion also coarsened the needle-like particles that can be associated with the brittle Fe-based Al_5FeSi intermetallics, based on the similarity between their morphology and that of the intermetallic phases revealed and discussed in [47]. Finally, the exposure of AB samples to 505 °C greatly enlarged the as-built α-Al grains as revealed by EBSD analysis and channelling contrast in [40,41,48,49]. The coarsening of the microstructure with prolonged exposure to the solutionizing temperature, along with a lower amount of alloying elements in the α-Al lattice [50], resulted in lower HV values of the SHT-4 with respect to the SHT-0.5 bare substrates (Fig. 2).

The subsequent exposure to the deposition temperature promoted precipitation phenomena in the SHT samples that recovered their HV values from 59÷75 $HV_{0.5}$ to 99÷110 $HV_{0.5}$. The HV values of both the T6–30 and T6–4 substrates, to the contrary, decreased slightly, following the same trends of the DA Al-Si-Mg bare samples, because, once again, the deposition process caused the material to exceed the peak-aging conditions attained during the T6 treatment, resulting in over-aging. Generally, the HV measurements in Fig. 2 are consistent with [41,51].

3.2. Microstructure and nanohardness of the DLC-based film

The SEM micrographs (Fig. 3 A-B) and the corresponding EDX analyses (Fig. 3C—D) confirmed that the architecture of the DLC-based films was independent of the substrate and consistent with the nominal one laid out in Section 2.1. A Cr adhesion layer (label 1 in Fig. 3 A – EDX spectrum 2 in Fig. 3C—D), ~0.5 µm thick, was deposited directly on the substrate surface. On top of it, the W-C:H layer, with a brighter bottom sub-layer (~0.25 µm) and a slightly darker upper sub-layer (~1 µm) provided a chemical and mechanical transition to the top DLC layer with a thickness of ~2.5 µm. The film was free of visible defects and followed the surface profile of the substrate. As specified in Section 2.2, because all substrates were coated under identical conditions, the microstructure of the film was observed only on selected specimens.

In the light of the thickness values quoted above, the results of the nanoindentation tests can be regarded as mainly representative of the properties of the DLC top layer, since the maximum penetration depth was less than 10% of the thickness of the DLC layer itself. The hardness and elastic modulus values, summarized in Table IV, were consistently unaffected by the substrate material and were comparable with the typical values for hydrogenated DLC (i.e., a-C:H layers) deposited by PA-CVD. Interestingly, the DLC layer had a hardness in excess of 2000 HV, but its elastic modulus was lower than that of ordinary steel. This means that the DLC top layer possessed good elastic compliance (high H/E ratio), which could be helpful to tolerate relatively large contact strains within the elastic deformation regime. In fact, since the substrates, whose profile the DLC-based films mostly copied, had Sq ≈ 0.06 µm and a mean asperity curvature Ssc ≈ 3×10^{-3} μm^{-1}, the plasticity index of

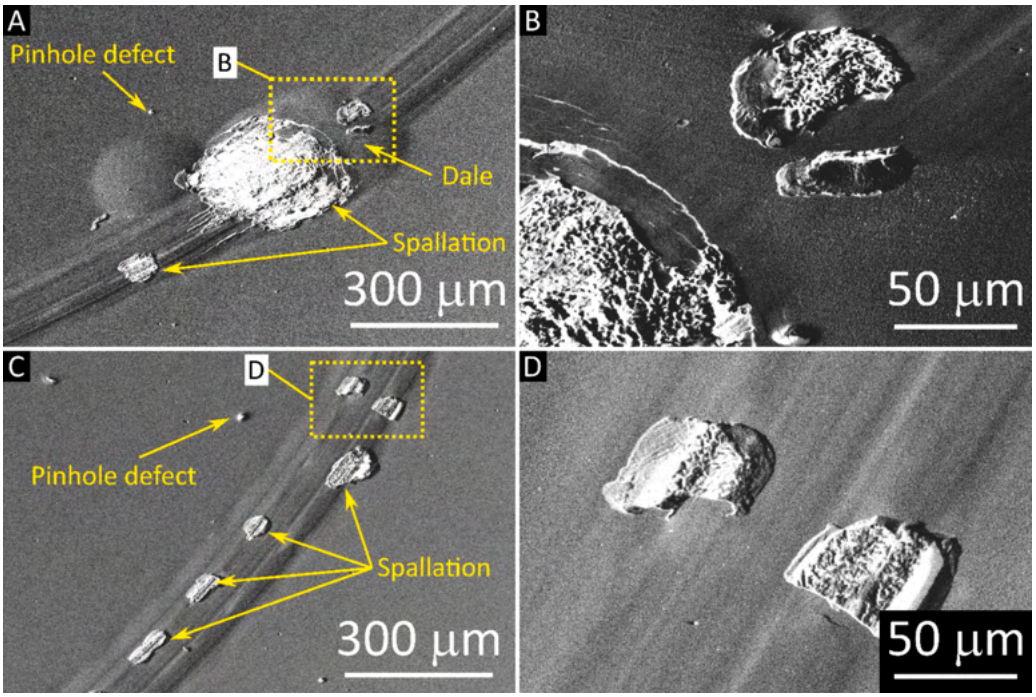

Fig. 17. EDX analyses acquired on the worn surface of the DLC-based film on the 10-DA-B (A-B) and 7-DA-T (C—D) samples.

the films, computed according to the original formulation by Greenwood and Williamson [52] as $\psi = (E/H) \bullet \sqrt{\sigma/R}$, where σ = standard deviation of the asperities' height distribution = Sq (when the reference plane is taken as the mean plane) and R = average curvature radius of the asperities = 1/Ssc, was $\psi \approx 0.1$. A plasticity index value $\psi \ll 1$ means that, at the microscale, the asperities of the DLC top layer would not reach their elasticity limit under contact conditions. When compared to the H/E values of other DLC-based films and PVD nitrides [53–56], the H/E ≈ 0.14 of the present DLC layer was indeed among the highest. Greater H/E values were only attained by special engineering of the film architecture [56]. Thus, the present results were promising, also in the light of the findings by Kasiorowski et al. [57], who showed that a PA-CVD DLC film with similar nanohardness (between 20.5 and 23.5 GPa) and elastic modulus (around 150 GPa) exhibited better sliding wear resistance than other types of DLC films with lower H/E ratios.

The W-C:H layer had a lower hardness but also an even lower elastic modulus, compared to the DLC top layer (Table IV), which resulted in a lower H/E ratio of around 0.09–0.10. Thus, under contact conditions, the W-C:H layer would be expected to reach the elastic limit before the DLC top layer.

The Raman spectra (Fig. 4) confirmed that the film had the signature spectrum of typical a-C:H type DLC. Fitting revealed that the ratio between the intensities of the D- and G-peaks (I(D)/I(G)) was 0.61 ± 0.02, and the G-peak position was 1542 ± 1 cm^{-1}. Based on the trends published by Ferrari and Robertson [58], these values indicate an sp^3 C—C bond fraction of around 45%. It should be reminded that, in a-C:H films, in addition to sp^2 C═C and sp^3 C—C bonds, C—H bonds also exist, but their signal is not meaningfully detectable in the Raman spectra [59]. The presence of hydrogen has a significant effect on the mechanical properties of DLC, because on the one hand it limits the continuity of the C—C network. Thus, it reduces the hardness and elastic stiffness of the film, compared with one having similar sp^2/sp^3 bond ratio but lower H content. On the other hand, hydrogen plays a major role during the PA-CVD deposition process, facilitating the formation of the sp^3 C—C bonds themselves [3]. Thus, in a standard PA-CVD process, the presence of hydrogen is indeed necessary to obtain a DLC material instead of a graphite-like coating. According to some authors, [59,60], the amount of hydrogen in a DLC film can be inferred from the slope of the raising background signal that it induces in the Raman spectrum through a photoluminescence effect. However, as seen in Fig. 4 A, the Raman spectra of the current samples did not exhibit a raising background. This could mean that the hydrogen content was below the threshold to observe a meaningful photoluminescence effect. This reportedly begins to show at about 34 at.% hydrogen content [60], albeit this is referred to a slightly lower excitation wavelength (514.5 nm) than was used in the present work (532 nm). Thus, our ability to excite the photoluminescence background may have been a bit lower and the threshold may have been correspondingly higher than the literature value. Nonetheless, we can infer that the DLC top layer had a limited H content, consistent with a typical a-C:H obtained by PA-CVD at a relatively high (in absolute value) bias voltage of −740 V (see Section 2.1) [3].

The full width of the G peak at half-maximum height (FWHM) was 187 ± 2 cm^{-1}, which, according to the plot by Casiraghi et al. [61] (though once again obtained for a slightly different excitation wavelength of 514.5 cm^{-1}), was fully consistent with an elastic modulus around 150 GPa as was found in Table IV.

3.3. Scratch adhesion of the DLC-based film on different substrates

The failure modes observed during the scratch test (Fig. 5) were quite typical of DLC-based films on metal substrates. Forward-facing fish-bone cracks started at L_{C1} due to the compressive stress ahead of the indenter. Chipping due to compressive destabilization of the film followed at L_{C2} and, at L_{C3}, the chipped areas extended enough to cover the entire width of the track; afterwards, delamination was triggered.

More in-depth inspection of the scratch tracks on the as-built AlSi10Mg substrates by SEM (Fig. 6A) confirmed that the DLC top layer experienced chipping along the edges (Fig. 6B) and, progressively, also toward the centre of the track (Fig. 6C). More interestingly, when the W-C:H layer was uncovered, it exhibited even more cracks than the DLC top layer itself. Fig. 6D indeed shows that, while some cracks extended across both the DLC top layer and the W-C:H layer, the latter also exhibited additional cracks, which tended to "disappear" beneath the surviving DLC top layer. It is thus inferred that, as long as the applied load was sufficiently low, most of the stress affected the DLC top layer and its own failure modes, dominated by compressive buckling,

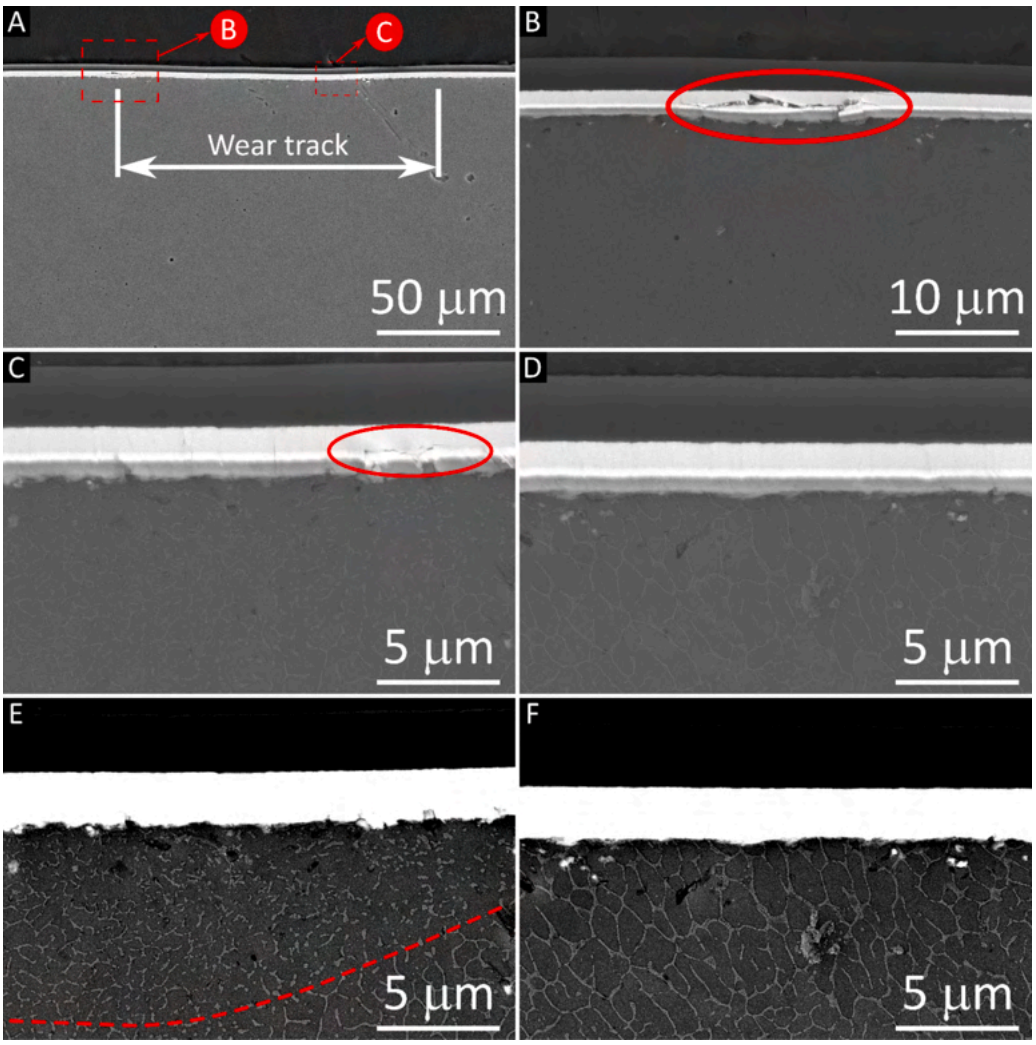

Fig. 18. SEM micrographs of the polished and etched cross-section of the coated 7-AB-T sample after the sliding wear test – A: overview around the wear track area; B, C: details of the areas marked in panel A, with circles highlighting cracks in the W-C:H layer; D: detail of an area outside the wear track; E, F: same as C and D but with digitally enhanced contrast to highlight the microstructure of the AlSi7Mg substrate. The dashed line in panel E indicates an area where the eutectic Si network of the as-built L-PBF alloy was disrupted by plastic deformation of the primary α-Al grains.

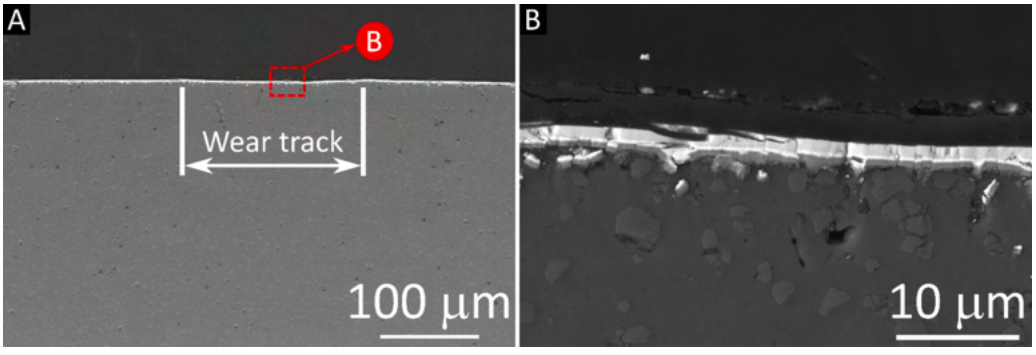

Fig. 19. SEM micrographs of the polished and etched cross-section of the coated 10-SHT-4 sample after the sliding wear test – A: overview around the wear track area; B: detail of the area marked in panel A.

appeared. However, when the load increased and more strain was put into the W-C:H interlayer, the latter was in fact the weakest link and started to crumble. Its failure then accelerated the spallation of the film and lead to the complete delamination as seen in Fig. 6A. This is consistent with the expectation, put forward in Section 3.2, that the W-C:H film would reach the elasticity limit at lower strain levels than the DLC film, thus exhibiting more extensive failure.

To verify the failure behaviour of the W-C:H layer alone, additional scratch tests were performed on as-built substrates coated only with the Cr / W-C:H system, as indicated in Section 2.1. The results showed that the critical load for continuous failure across the track width (L_{C3}) and the delamination load ($L_{Delam.}$) were indeed lower for the W-C:H-

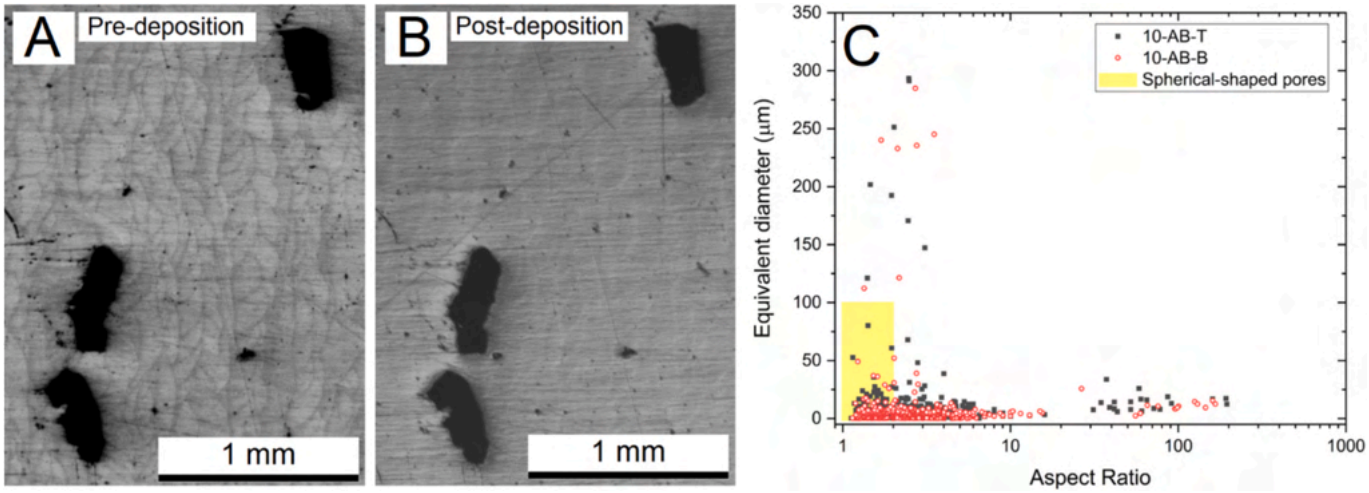

Fig. 20. OM micrographs of bare (A) and coated (B) 10-AB-T substrates and the equivalent diameters of spherical- and irregular-shaped pores in function of their aspect ratio (C) analysed in 10-AB samples.

terminated coating system than for the complete DLC-based film (Table V). The failure modes were also different (Fig. 7): the W-C:H layer confirmed its tendency to crumble at high loads, developing an extensive network of through-thickness cracks (Fig. 7B) that uncovered increasingly wide portions of the substrate (Fig. 7C).

Thus, the W-C:H layer likely started to crack and tear in the same way also underneath the DLC top layer in the complete coating system, accelerating its failure. Detailed views showed that the Cr adhesion layer was firmly attached to the W-C:H layer (Fig. 7D), confirming that the W-C:H layer, not the adhesion layer, was the actual weakest part of the coating system.

Considering now the evolution of the critical loads of the DLC-based films as a function of the substrate treatment condition (Fig. 8), some interesting trends emerged. In particular, the average values of the delamination load ($L_{Delam.}$) decreased continuously going from as-built substrates to direct aged, solution treated, and T6 substrates. This result can be directly visualized through the optical micrographs of the scratch tracks (Fig. 5), from which the critical loads were measured. The change in delamination loads is apparent through the emergence of the metallic shine of the uncovered substrate in the different scratch tracks. The difference between the average $L_{Delam.}$ values measured on the as-built and direct-aged samples was, in most cases, smaller than the associated error ranges; hence, it was hardly significant from a statistical point of view. Nonetheless, the differences recurred systematically with both substrate materials and regardless of the distance from the heated build platform, namely with both the top and the bottom samples. There was a marked decrease of the $L_{Delam.}$ values after the solution treatment and, even more, after the T6 treatment. The trends with all other critical load values were analogous, but going toward lower load values, the differences became increasingly small and, therefore, less significant. Interestingly, the delamination load of the DLC-based films on the AlSi10Mg substrates seemed a bit higher than that of the films on the AlSi7Mg substrates in the as-built condition, but a bit lower after the solution treatment and the T6 treatment (Fig. 8), though the difference was not particularly significant.

This different mechanical behaviour may be based on the different responses to mechanical loads supported by the networked microstructure (AB and DA samples in Fig. 1 A) and the composite-like one (Fig. 1B,C), along with the influences dictated by the precipitates formed within the α-Al matrix. As widely investigated in [62], the mechanical behaviour of the AB and DA substrates was almost completely governed by the Si-eutectic network, which was extended as a tubular structure from the bottom to the top region of the sample, regardless of the precipitate amount within the α-Al cells. Based on these reasons, AlSi10Mg substrates could exhibit higher delamination loads likely due presence of a denser eutectic network compared to the AlSi7Mg substrates. This statement can be supported by the smaller dimensions of the α-Al cells in AlSi10Mg compared to AlSi7Mg substrates (see Table III). In fact, for the same substrate's area, a denser structure of the Si eutectic network contains less space where α-Al can be enclosed. Focusing on the composite microstructure of the SHT and the T6 substrates, the precipitates formed in the α-Al matrix after aging greatly affect the mechanical behaviour and the mechanical load bearing capability of the Al-Si-Mg alloys [62]. For these reasons, the slightly higher delamination load of AlSi7Mg substrates may be caused by the higher precipitate amount within the matrix compared to the AlSi10Mg substrates, whereas the role of the Si particles was diminished by the destruction of the above-mentioned network. In fact, the AlSi7Mg alloy contained twice the amount of Mg compared with the AlSi10Mg alloy (see Table I), which played a key role in the precipitate formation during exposure to aging temperatures.

The identification of the $L_{Delam.}$ values was also corroborated by the instrumental recordings during the scratch test. In fact, the delamination events were accompanied by a transition from a low-friction regime (Fig. 9) to higher and more unstable friction coefficient values as the indenter passed from sliding onto the DLC-based film to sliding onto the bare Al alloys. The total and residual penetration depths also exhibited sudden increases corresponding to the occurrence of delamination. All these shifts occurred around a load of 15 N with the AB substrates and at a marginally lower load with the DA substrates; they moved toward a value of 10 N with SHT and T6 samples (Fig. 9).

These findings strongly suggest that the critical loads were closely related to the hardness of the substrate. Fig. 10 confirms that there was indeed a linear relation between all critical loads and the hardness of the corresponding substrates, with quite high R^2 values in the range of 0.61÷0.84, particularly for the delamination load.

It is interesting to note that the friction coefficient measured before the delamination event (Fig. 9) did not remain constant but increased continuously from ~ 0.1, at the beginning of the test to ~ 0.25, shortly before the critical load, which was an apparent violation of Amontons' laws, according to which the friction coefficient should be independent of the apparent contact area and the normal load. One reason can be a non-linearity in the adhesive contribution to friction. The latter is a monotonic function of the τ_m/H ratio [63,64], where τ_m is the maximum shear strength of the adhesive junctions formed between contacting asperities, and H is the hardness of the softer surface, that is, in the present tests, the coated sample. The shear strength is proportional to the work of adhesion: $\tau_m \propto W_{12} \approx c \bullet (\gamma_1 + \gamma_2)$, where c = chemical

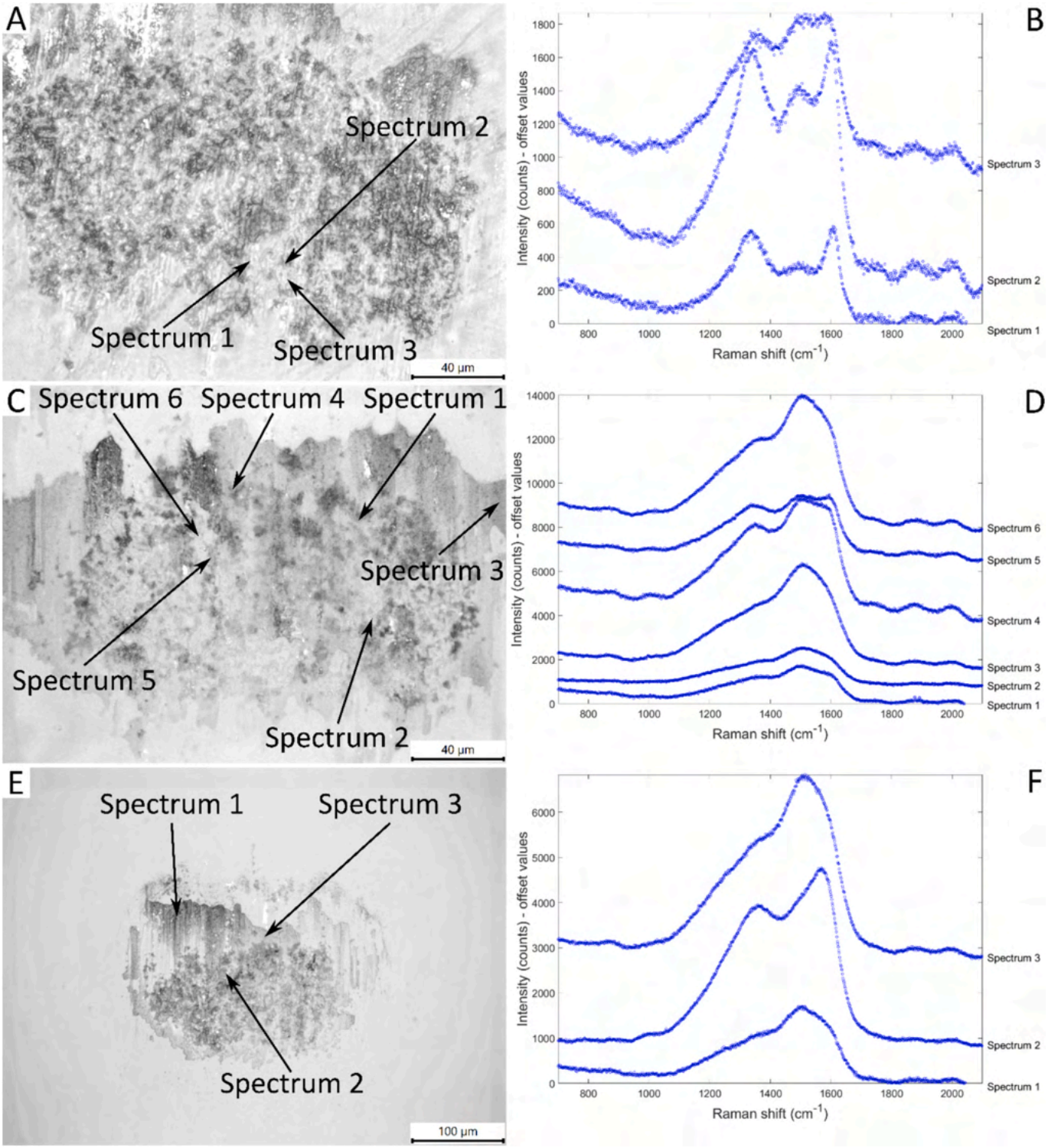

Fig. 21. Optical micrographs of the Al_2O_3 balls after wear testing against the DLC-based films on the 7-AB-B (A), 7-AB-T (C), and 7-SHT-4 (E) samples, with corresponding Raman spectra (B, D, F) acquired at the marked locations.

compatibility; γ_1, γ_2 = surface energies of the mating surfaces [63]. Because hydrogenated DLC [3,5] and diamond both possessed low surface energy, τ_m was low and independent of the applied load. However, under an increasingly high normal load, the contact stress distribution extended further into the soft Al-alloy substrate. Thus, the effective hardness of all samples (H) decreased with increasing load, resulting in a continuous increase in the τ_m/H ratio that reflected a more-than-linear increase of the true contact area with the applied normal load. Furthermore, because the substrate was deforming plastically during the scratch test, dissipating energy in the process, there was also an abrasive contribution to friction. To a first approximation, the abrasive contribution to friction increases with $\tan\theta$, where θ is the attack angle of the abrading asperity [63]. With a spherical indenter, the average attack angle increased with the penetration depth, thus resulting in an increase of the abrasive contribution to friction.

As for the scratch test results, the different microstructures and

hardness values characterizing the AB, DA, SHT, and T6 substrates greatly influenced the damage to the coating after Rockwell indentations (Fig. 11), as well. In fact, both the radial cracks and the delamination areas in the coating increased when changing from Al-Si-Mg substrates with a networked microstructure (AB, DA) to those showing a composite-like structure (SHT, T6) (Fig. 11 A). In detail, with a Si-eutectic network in the substrate, almost only cracking phenomena were induced in DLC coating, likely because the tubular microstructure supported the coating, as previously discussed. On the contrary, the lack of support induced by the composite-like microstructure (Fig. 11C) resulted in the appearance of small delamination areas (Fig. 11B,C). The aspects will be corroborated through the dry sliding wear results in Section 3.4.

Confirming that the delamination events in the Rockwell VDI test and the scratch test were related to the same mechanisms associated with the mechanical support from the substrate, Fig. 12 shows a definite correlation between the reduction in critical loads and the increase in the area fraction of delaminated coating around the indentation mark.

Despite the appearance of small delamination damage with the SHT and T6 substrates, the response of the DLC-based coating should always be ascribed to the HF2 adhesion class, because the delamination areas were not observable at the lower magnification level required to match the observed Rockwell imprint in Fig. 11B with the failure chart in Fig. 11D. The low-magnification OM micrograph in Fig. 11B is thus representative of all analysed conditions. In this context, it is interesting to note that the more detailed analysis carried out on the damages induced by the Rockwell VDI test revealed worse adhesion classes. In fact, considering that the entire Rockwell imprint should be compared with the failure chart (Fig. 11D).

3.4. Dry sliding wear behaviour of the coated systems

The results of all dry sliding wear tests (Table VI) show that the specific wear rates of the coatings deposited on the as-built samples were mostly $<1 \times 10^{-6}$ mm^3/(N•m), i.e., corresponding to a moderate wear regime [65]. The friction coefficient was also low, around 0.12–0.13, which fell within the typical range of the friction coefficient values produced by hydrogenated DLC films sliding against most types of counterbodies in humid air [5]. There was no apparent effect of either the exact composition (AlSi10Mg or AlSi7Mg) or the position with respect to the build platform. In a few cases, however, the scatter in the data was quite large, as in the second replicates of the wear test on the 10-AB-T and the 10-AB-B samples (Table VI). In the latter case, one of the four profile measurements was not included in the averaging because the cross-sectional area measured at that location (see the procedure described in Section 2.4) was almost one order of magnitude higher than the other three measurements.

Moving to the direct aged and the solutionized samples, the scatter increased further. In some tests, the specific wear rates were as low as for the as-built samples; others returned higher averages with large scatter, such as the first replicate on sample 10-DA-B and both replicates of sample 7-SHT-4; and in yet other cases, the coating delaminated completely before the end of the test, uncovering the Al-alloy substrate. The delamination event was clearly identifiable through the friction curves (Fig. 13), where a sharp transition from a low-friction regime to a high and unstable friction (e.g. see in curve 1 in panel C, curve 2 in panel D, and both curves in panels G and H) marked the contact between the ball and the metal substrate, which suffered severe adhesive wear. The approximate distances where this event occurred are listed in Table IV.

All coatings on the T6 substrates delaminated before the end of the test (Fig. 13G,H), and, especially with the AlSi10Mg substrates, the delamination event occurred early on, after a few hundred meters of sliding.

Some considerations can therefore be made. The frequency of highly scattered wear data or delamination events increased with decreasing hardness of the substrate. Thus, scattered data and delamination events were more frequent as the critical loads measured by scratch tests decreased. Even the poorer performance of the 10-T6 samples, where the coating delaminated earlier than on the corresponding 7-T6 substrates, and of the 10-SHT samples, where the coating delaminated in two out of four repetitions (considering both the 30′ and the 4 h duration of the solution treatment) and after a shorter distance, as opposed to one single delamination event after a longer distance with the 7-SHT substrates, were consistent with the slight difference noted between the respective scratch test results (Fig. 8).

It is logical that an excessive loss of substrate hardness (Fig. 2), resulting in a too low critical load in the scratch test (Figs. 8 and 10), would cause systematic delamination of the coating, as it indeed occurred with the T6 samples. The fact that, at intermediate levels of substrate hardness and scratch adhesion, the behaviour of the coatings became highly scattered is less intuitive and deserves a more in-depth explanation through an analysis of the wear mechanisms.

SEM inspection of the worn samples revealed three different morphologies:

1) Some areas along the wear tracks exhibited no major damage, with only minor polishing wear. The fine-scale roughness of the DLC film was removed, and shallow grooves were developed (Figs. 14A-B, 15A-B and 16A-B).
2) On the as-built samples, there were local spallations of the film (Figs. 14E-F and 15E-F) scattered along the wear track. With the direct aged and the solution treated substrates, the spallations sometimes degenerated from their onset location into an extended damage affecting an entire section of the wear track (Fig. 16C-D).
3) Occasionally, the wear track passed through large dales on the coated surface. The dales were so deep that, in their centre, they did not exhibit any sign of contact: the ball bridged from one edge of the dale to the other, without touching the middle part (Figs. 14C-D and 15C-D). This resulted in a large stress concentration on the edge facing the direction of relative motion, usually triggering a large delamination event. Again, with the direct aged and solution treated substrates, the delamination that started at the edge of a dale tended to extend along an entire portion of the wear track, as exemplified by Fig. 16E-F. It is most likely that the dales corresponded to open pores on the polished surface of the L-PBF samples. This was particularly apparent in Fig. 16F, where unmelted powder particles could be seen within the dale. This means that the specific dale seen in this micrograph was a lack-of-fusion defect. In other cases, broader and more rounded dales might come from gas pores in the LPBF substrate.

EDX spectra indicated that the delaminated areas initially exposed the WC-based underlayers (Fig. 17A-B: spectrum 1; Fig. 17C-D: spectra 1, 3, 5, and 6). Successive damage after the initial delamination presumably removed the remaining coating layers and exposed the Al-based substrate (Fig. 17A-B: spectra 2, 3, and 5).

The cross-section of the worn 7-AB-T sample showed further important features:

i) The formation of the wear track was not due to actual wear of the DLC-based film, whose thickness looked practically unchanged compared to the outer surface (Fig. 18A,B). The depression identified and quantified by profilometry was, in fact, mainly the consequence of plastic deformation of the Al alloy substrate under the contact stress (Fig. 18A). Thus, it is inferred that the true wear rate of the coating was far lower than the values reported in Table IV. Accordingly, Kasiorowski et al. [57] reported specific wear rates of the order of 10^{-8} mm^3/(N•m) when a PA-CVD film having comparable hardness, elastic modulus, and fraction of sp^3-bonded carbon was deposited on quenched-and-tempered medium-carbon steel, with or without a nitriding treatment, since the steel substrate did not deform plastically under load and thus the measured volume of the wear track reflected the actual wear loss from the coating. It is likely that the “intrinsic” wear rate of the present

films was of the same order. Looking back at the top-surface SEM views, it can also be noted that the abrasive grooves along the DLC top layer continued in the WC-based underlayers when the latter were exposed by small spallation events, such as in Fig. 14F. This means that the grooves were, in fact, due to plastic deformation of the substrate under the coating and not to abrasive removal of the coating material itself. As mentioned in Section 2.4, the hertzian contact stress distribution, which was only moderately altered by the additional contribution of frictional stresses on account of the low friction coefficient, had its maximum within the substrate and exceeded its yield strength. Enhancing the contrast of the cross-sectional micrographs to visualize the etched microstructure of the substrate (Fig. 18E,F) showed that, outside the wear track (Fig. 18F), the as-built Al-Si-Mg alloys possessed a fine cellular microstructure typical of the LPBF process. Directly below the wear track, down to a depth of some micrometres, that microstructure was altered (Fig. 18E: see the area delimited by the dashed line): the primary α-Al grains flowed plastically under the contact stress and the surrounding network of eutectic Si was consequently disrupted.

ii) There were cracks in the W-C:H layer and at its interface with the Cr layer (Fig. 18B,C: circled areas), even in the absence of visible cracks in the DLC layer. Therefore, it was inferred that even the harder as-built substrates could not prevent plastic deformation under the severe contact stresses intentionally imposed by the chosen wear test conditions. Thus, the DLC-based film was forced to follow the plastic flow of the substrate, subjecting it to a quite critical condition. The high H/E ratio of the DLC top layer (Section 3.2) meant that it had a good ability to accommodate elastic deformations; for example, McMaster et al. [66] showed a linear decrease in the fretting wear rate of DLC-based films with increasing H/E ratio. However, the W-C:H layer has a lower H/E ratio, indicating a lower elastic strain limit (Section 3.2). Therefore, just as it happened in the scratch tests (Section 3.2, Figs. 6 and 7), the cross-sectional views of the worn samples indicated that, in fact, it was the W-C:H layer that started to crack. Hence, the W-C:H layer was confirmed to be the weak link in the DLC-based coating system. It is reasonable to conclude that the localized spallations seen in Figs. 14E-F and 15E-F were caused by such cracking of the W-C:H layer: when the cracks extended further and climbed to the top surface, a coating fragment was detached. The reason why they appeared at some locations and not at others was probably associated with the random presence of small defects in the coating. When this critical condition was coupled with further stress concentration associated with large defects on the substrate surface, then wider delaminations were produced.

A decrease in the hardness of the Al alloys resulting from heat treatments (Fig. 2) at increasingly high temperatures enabled even larger plastic strains in the substrate. Fig. 19 accordingly showed that the W-C:H layer on the solution treated substrate was more extensively cracked. The layer was so extensively fragmented that loose pieces produced by sectioning were then pushed into the substrate during the polishing procedure. The W-C:H layer cracked particularly when the coating touched the aluminium matrix, whilst, when the coating was in contact with one of the coarse Si particles, this phenomenon was limited (Fig. 19B). As a result of the more extensive damage of the W-C:H layer on softened substrates, the delamination areas on the surface of the coating grew larger and tended to propagate from an initial starting point, as noted above (Fig. 16C-D). Likewise, the damage produced when the wear track crossed a defect on the substrate surface also grew larger when the substrate became softer (Fig. 16E-F). It is likely that, when the track crossed particularly large and/or numerous defects, the result was a complete delamination of the coating. The randomness of the distribution of such defects explained the uneven occurrence of the delamination events with the direct aged and the solutionized samples (Table IV).

Fig. 20 corroborates the conclusion on the defect-correlated damages during the wear test considering that bare substrates (Fig. 20A) were characterized by a high amount of both circle-shaped gas pores (aspect ratio < 2 and equivalent diameter ≤ 100 μm [67], Fig. 20C) and irregular-shaped lack-of-fusion pores (Fig. 20C), which were not filled by the DLC-coating during the deposition process. In this context, it is useful to note that pores with a size smaller than the thickness of the DLC film (2.5 μm, see Fig. 3) were completely covered (compare Fig. 20A and B). Tillmann et al. [68] exhibited the ability of the PVD process to coat pores with relatively large size and limited depth with respect to the size. In such cases, the coating morphology closely follows that of the pore. The same authors also demonstrated that, for pores characterized by significant depth, the PVD process is unable to fully cover the pore, but instead leads to a reduction in the effective pore size. This latter scenario describes all lack-of-fusion defects visible in Fig. 20A,B, where a clear reduction in their size is observed after deposition of the DLC film. Both gas and lack-of-fusion pores were randomly distributed within the bare substrates due to the working conditions of LPBF process.

Thus, the interplay between the critical operating conditions of the coating under contact conditions that trigger plastic deformation of the substrate, and the random distribution of defects on the substrate surface, was the explanation for the variability observed in the results and was the reason why delamination of the wear track occurred on some of the direct aged and solution treated samples, but not others. With the T6 treatment, which caused the greatest drop in hardness and the correspondingly largest decrease in the critical load, the contact conditions were so severe that delamination happened in every case, regardless of the presence of localized defects.

To rule out any anomalies in the tribological behaviour of the DLC coating, which in fact, based on the previous analysis, exhibited an excellent intrinsic wear resistance, we also examined the nature of the transfer film on the counterbody in tests where the wear track did not exhibit excessively large spallations or complete delamination. Optical micrographs (Fig. 21 A, C, E) show that the counterbody did not exhibit any meaningful wear, and was just covered by a film which, based on Raman spectra acquired at different positions (Fig. 21B, D, F), was made of fine DLC debris with varying degrees of graphitization. This was indeed the expected tribological behaviour of DLC films and explained the low friction regime observed in the wear tests (Fig. 13 and Table IV).

4. Conclusions

The characterization of the adhesion and ball-on-disc sliding wear behaviour of DLC-based films deposited onto LPBF AlSi7Mg and AlSi10Mg substrates in different treatment conditions (as-built, direct aged, solution-treated, and T6) led to the following conclusions:

- Aging of the Al alloys during the combined PVD / PA-CVD process carried out at 175 °C removed any perceivable difference between the microstructure and hardness of substrates grown close to or far from the build platform. It also resulted in the solution-treated samples becoming harder than the T6 ones, since the former were aged during deposition whilst the latter experienced over-aging.
- The scratch adhesion of the coatings, which could be effectively characterized through the critical load for delamination, was linearly correlated with the hardness of the substrate. Likewise, the fraction of delaminated coating area around a Rockwell indentation increased with decreasing substrate hardness, and showed a correlation with the critical load for delamination.
- During sliding wear tests carried out with high initial contact pressure, all Al-alloy substrates experienced plastic deformation. Most of the apparent volume lost from the wear track was therefore due to plastic displacement of the substrate material, whilst the actual reduction in thickness of the coating was minimal.
- The DLC-based top layer had a high H/E ratio of about 0.14, which meant it had some ability to follow elastically the deformation of the substrate. However, the underlying W-C:H intermediate layer started to crack during the wear test. When these cracks grew and climbed to the surface, the film was locally spalled. When the hardness of the

substrate decreased, damage to the W-C:H interlayer became more severe and the spalled areas grew larger.
- Open pores were scattered across the surface of the polished LPBF substrates. When the ball-on-disc wear track intercepted a pore, a contact stress concentration ensued, which led to larger local spallations of the film.
- The interplay between the greater tendency of the film to spall when deposited on softer substrates and the random presence of open pores that promote increasingly large damage meant that the DLC-based film occasionally delaminated from the entire wear track during the tests with direct-aged or solution-treated substrates. Thus, the net result of a decreased substrate hardness was a loss in reliability of the coated system.
- With the highly softened T6 substrates, the coating always delaminated under the present test conditions.

Ultimately, it can be concluded that the direct deposition of a DLC-based film on an LPBF substrate is not recommended for highly loaded contact conditions. Nonetheless, the use of as-built substrates can produce satisfactory tribological performances even in rather severe conditions. The role of open pores in a polished LPBF samples also seems to be of particular importance, and future work might be dedicated to exploring systematic correlations between porosity (which results from the LPBF parameters) and tribological performance (particularly the reliability of the coated systems).

CRediT authorship contribution statement

Maria Francesca Bonilauri: Writing – review & editing, Writing – original draft, Visualization, Validation, Investigation, Formal analysis, Data curation. **Emanuele Ghio:** Writing – review & editing, Writing – original draft, Visualization, Validation, Supervision, Resources, Project administration, Investigation, Funding acquisition, Formal analysis, Data curation, Conceptualization. **Giovanni Bolelli:** Writing – review & editing, Writing – original draft, Visualization, Validation, Supervision, Resources, Project administration, Investigation, Formal analysis, Data curation, Conceptualization. **Bertè Alessandro:** Writing – review & editing, Writing – original draft, Resources. **Emanuela Cerri:** Writing – review & editing, Writing – original draft, Validation, Supervision, Resources, Project administration, Funding acquisition, Conceptualization.

Declaration of competing interest

The authors declare the following financial interests/personal relationships which may be considered as potential competing interests: Emanuele Ghio reports financial support was provided by both Italian Ministry of University and Research. Alessandro Bertè reports a relationship with Lafer S.p.A. that includes: employment.

Acknowledgements

The project was founded under the National Recovery and Resilience Plan (NRRP), Mission 4, Component 2, Investment 1.5. – Call for tender No. 3277 of 30/12/2021 of Italian Ministry of University and Research funded by European Union – NextGenerationEU.

Data availability

Data will be made available on request.

References

[1] J. Robertson, Classification of diamond-like carbons, in: C. Donnet, A. Erdemir (Eds.), Tribology of Diamond-like Carbon Films, Springer US, Boston, MA, 2008, pp. 13–24, https://doi.org/10.1007/978-0-387-49891-1_1.
[2] A. Matthews, S.S. Eskildsen, Engineering applications for diamond-like carbon, Diam. Relat. Mater. 3 (1994) 902–911, https://doi.org/10.1016/0925-9635(94)90297-6.
[3] J. Robertson, Diamond-like amorphous carbon, Mater. Sci. Eng. R. Rep. 37 (2002) 129–281, https://doi.org/10.1016/S0927-796X(02)00005-0.
[4] A. Erdemir, Solid lubricants and self-lubricating films, in: B. Bhushan (Ed.), Modern Tribology Handbook, Two Volume Set, CRC Press, Boca Raton, FL, 2001, pp. 787–825. http://search.ebscohost.com/login.aspx?direct=true&db=nlebk&AN=154300&site=ehost-live&scope=site.
[5] H. Ronkainen, K. Holmberg, Environmental and thermal effects on the Tribological performance of DLC coatings, in: C. Donnet, A. Erdemir (Eds.), Tribology of Diamond-like Carbon Films, Springer US, Boston, MA, USA, 2008, pp. 155–200, https://doi.org/10.1007/978-0-387-49891-1_6.
[6] S.V. Hainsworth, N.J. Uhure, Diamond like carbon coatings for tribology: production techniques, characterisation methods and applications, Int. Mater. Rev. 52 (2007) 153–174, https://doi.org/10.1179/174328007X160272.
[7] A. Grill, Tribology of diamondlike carbon and related materials: an updated review, Surf. Coat. Technol. 94–95 (1997) 507–513, https://doi.org/10.1016/S0257-8972(97)00458-1.
[8] R. Ferreira, J. Martins, Ó. Carvalho, L. Sobral, S. Carvalho, F. Silva, Tribological solutions for engine piston ring surfaces: an overview on the materials and manufacturing, Mater. Manuf. Process. 35 (2020) 498–520, https://doi.org/10.1080/10426914.2019.1692352.
[9] S.C. Tung, V. Wong, Surface engineering development trends and impact of surface coatings and textures on automotive powertrain friction and Wear control, Mater. Perform. Char. 10 (2021) 620–650, https://doi.org/10.1520/MPC20200091.
[10] R. Hauert, An overview on the tribological behavior of diamond-like carbon in technical and medical applications, Tribol. Int. 37 (2004) 991–1003, https://doi.org/10.1016/j.triboint.2004.07.017.
[11] K. Malisz, B. Świeczko-Żurek, A. Sionkowska, Preparation and characterization of diamond-like carbon coatings for biomedical applications—a review, Materials 16 (2023) 3420, https://doi.org/10.3390/ma16093420.
[12] W.S. Miller, L. Zhuang, J. Bottema, A.J. Wittebrood, P. De Smet, A. Haszler, A. Vieregge, Recent development in aluminium alloys for the automotive industry, Mater. Sci. Eng. A 280 (2000) 37–49, https://doi.org/10.1016/S0921-5093(99)00653-X.
[13] L. Zhu, N. Li, P.R.N. Childs, Light-weighting in aerospace component and system design, Propulsion Power Res. 7 (2018) 103–119, https://doi.org/10.1016/J.JPPR.2018.04.001.
[14] H. Dong, Tribological properties of titanium-based alloys, in: H. Dong (Ed.), Surface Engineering of Light Alloys, Elsevier, 2010, pp. 58–80, https://doi.org/10.1533/9781845699451.1.58.
[15] H.J. Spies, Surface engineering of aluminium and titanium alloys: an overview, Surf. Eng. 26 (2010) 126–134, https://doi.org/10.1179/174329409X451146.
[16] R.Y.Q. Fu, Duplex surface treatments of light alloys, in: H. Dong (Ed.), Surface Engineering of Light Alloys, Elsevier, 2010, pp. 501–545, https://doi.org/10.1533/9781845699451.2.501.
[17] K. Holmberg, H. Ronkainen, A. Matthews, Tribology of thin coatings, Ceram. Int. 26 (2000) 787–795, https://doi.org/10.1016/S0272-8842(00)00015-8.
[18] H. Ronkainen, J. Koskinen, S. Varjus, K. Holmberg, Load-carrying capacity evaluation of coating/substrate systems for hydrogen-free and hydrogenated diamond-like carbon films, Tribol. Lett. 6 (1999) 63–73, https://doi.org/10.1023/A:1019107622768.
[19] K. Holmberg, A. Laukkanen, H. Ronkainen, K. Wallin, S. Varjus, J. Koskinen, Tribological contact analysis of a rigid ball sliding on a hard coated surface: part II: material deformations, influence of coating thickness and young's modulus, Surf. Coat. Technol. 200 (2006) 3810–3823, https://doi.org/10.1016/J.SURFCOAT.2005.03.041.
[20] K. Holmberg, A. Laukkanen, H. Ronkainen, K. Wallin, S. Varjus, J. Koskinen, Tribological contact analysis of a rigid ball sliding on a hard coated surface: part I: modelling stresses and strains, Surf. Coat. Technol. 200 (2006) 3793–3809, https://doi.org/10.1016/J.SURFCOAT.2005.03.040.
[21] C.T. Wang, T.J. Hakala, A. Laukkanen, H. Ronkainen, K. Holmberg, N. Gao, R.J.K. Wood, T.G. Langdon, An investigation into the effect of substrate on the load-bearing capacity of thin hard coatings, J. Mater. Sci. 51 (2016) 4390–4398, https://doi.org/10.1007/s10853-016-9751-8.
[22] E. Ghio, G. Bolelli, A. Bertè, E. Cerri, Diamond-like carbon (DLC) and AlCrN films onto Ti-6Al-4V substrates by laser-powder bed fusion (L-PBF): effect of substrate heat treatment and surface finish, Surf. Coat. Technol. 475 (2023) 130128, https://doi.org/10.1016/J.SURFCOAT.2023.130128.
[23] G. Di Egidio, C. Martini, L. Ceschini, A. Morri, Influence of Electroless nickel—DLC (diamond-like carbon) multilayer coating on the mechanical performance of the heat-treated AlSi10Mg alloy produced by powder bed fusion-laser beam, Materials 16 (2023) 3313, https://doi.org/10.3390/ma16093313.
[24] G. Di Egidio, C. Martini, E. Ghassemali, A. Morri, Electroless Ni-P + diamond-like carbon multilayer: influence on tribological behaviour of AlSi10Mg produced by powder bed fusion - laser beam, Wear 566–567 (2025) 205803, https://doi.org/10.1016/J.WEAR.2025.205803.
[25] I. Gibson, D. Rosen, B. Stucker, Powder Bed Fusion Processes, in: Additive Manufacturing Technologies, Springer New York, New York, NY, 2015, pp. 107–145, https://doi.org/10.1007/978-1-4939-2113-3_5.
[26] S. Sun, M. Brandt, M. Easton, Powder bed fusion processes, in: M. Brandt (Ed.), Laser Additive Manufacturing, Elsevier - Woodhead Publishing, 2017, pp. 55–77, https://doi.org/10.1016/B978-0-08-100433-3.00002-6.
[27] M. Leary, Surface roughness optimisation for selective laser melting (SLM), in: M. Brandt (Ed.), Laser Additive Manufacturing, Elsevier - Woodhead Publishing,

Duxford, UK, 2017, pp. 99–118, https://doi.org/10.1016/B978-0-08-100433-3.00004-X.
[28] E. Salerno, D. Casotti, G. Paolicelli, E. Gualtieri, A. Ballestrazzi, G.C. Gazzadi, G. Bolelli, L. Lusvarghi, S. Valeri, A. Rota, Friction and wear of DLC films deposited on additive manufactured AlSi10Mg: the role of surface finishing, Surf. Coat. Technol. 463 (2023) 129531, https://doi.org/10.1016/j.surfcoat.2023.129531.
[29] E. Ghio, M.F. Bonilauri, G. Bolelli, P. Colombi, E. Cerri, A Novel Approach to Rockwell and Scratch Adhesion Tests for Hard Coatings Deposited onto Ti6Al4V Substrates, Metals 15 (2025) 994, https://doi.org/10.3390/MET15090994.
[30] F.O. Kolawole, S.K. Kolawole, L.B. Varela, A. Kraszczuk, M.A. Ramirez, A. P. Tschiptschin, Effect of substrate surface roughness on the tribological properties of dlc-h coatings on tappet valve, Tribol. Industry 43 (2021) 189–199, https://doi.org/10.24874/TI.927.07.20.11.
[31] S.A. Khan, J. Oliveira, F. Ferreira, N. Emami, A. Ramalho, Surface roughness influence on Tribological behavior of HiPIMS DLC coatings, Tribol. Trans. 66 (2023) 565–575, https://doi.org/10.1080/10402004.2023.2197472.
[32] P.S. Martins, S.S. Pires, E. Rodrigues da Silva, V.F. Vieira, E.C. Talibouya Ba, C. A. Rodrigues Dias, Tribological aspects of the diamond-like carbon film applied to different surfaces of AISI M2 steel, Wear 506–507 (2022) 204469, https://doi.org/10.1016/J.WEAR.2022.204469.
[33] D. Sheeja, B.K. Tay, H.M. Lam, S.K. Ng, EFFECT OF SURFACE ROUGHNESS ON THE ADHESIVE AND TRIBOLOGICAL CHARACTERISTICS OF DLC COATING PREPARED ON co-Cr-Mo ALLOY, Int. J. Mod. Phys. B 16 (2002) 952–957, https://doi.org/10.1142/S021797920201066X.
[34] A.K. Mishra, A. Kumar, Effect of process parameters on melt Pool characteristics and solidification process during laser powder bed fusion of AlSi10Mg alloy, Lasers Manufact. Mater. Proc. 11 (2024) 260–283, https://doi.org/10.1007/s40516-023-00243-4.
[35] S. Dong, X. Zhang, F. Ma, J. Jiang, W. Yang, Research on deposited tracks and microstructures of AlSi10Mg alloy produced by selective laser melting, Appl. Phys. A 126 (2020) 643, https://doi.org/10.1007/s00339-020-03826-6.
[36] G. Di Egidio, C. Martini, J. Börjesson, E. Ghassemali, L. Ceschini, A. Morri, Influence of microstructure on fracture mechanisms of the heat-treated AlSi10Mg alloy produced by laser-based powder bed fusion, Materials 16 (2023) 2006, https://doi.org/10.3390/ma16052006.
[37] L. Song, L. Zhao, L. Ding, Y. Zhu, M. Huang, A. Simar, Z. Li, Microstructure and loading direction dependent hardening and damage behavior of laser powder bed fusion AlSi10Mg, Mater. Sci. Eng. A 832 (2022) 142484, https://doi.org/10.1016/J.MSEA.2021.142484.
[38] A. Hadadzadeh, B.S. Amirkhiz, B. Langelier, J. Li, M. Mohammadi, Microstructural consistency in the additive manufactured metallic materials: a study on the laser powder bed fusion of AlSi10Mg, Addit. Manuf. 46 (2021) 102166, https://doi.org/10.1016/J.ADDMA.2021.102166.
[39] P. Van Cauwenbergh, V. Samaee, L. Thijs, J. Nejezchlebová, P. Sedlák, A. Iveković, D. Schryvers, B. Van Hooreweder, K. Vanmeensel, Unravelling the multi-scale structure–property relationship of laser powder bed fusion processed and heat-treated AlSi10Mg, Sci. Rep. 11 (2021) 1–15, https://doi.org/10.1038/s41598-021-85047-2.
[40] S. Zhu, I. Katti, D. Qiu, J.H. Forsmark, M.A. Easton, Microstructural analysis of the influences of platform preheating and post-build heat treatment on mechanical properties of laser powder bed fusion manufactured AlSi10Mg alloy, Mater. Sci. Eng. A 882 (2023) 145486, https://doi.org/10.1016/j.msea.2023.145486.
[41] H. Zhang, Y. Wang, J.J. Wang, D.R. Ni, D. Wang, B.L. Xiao, Z.Y. Ma, Achieving superior mechanical properties of selective laser melted AlSi10Mg via direct aging treatment, J. Mater. Sci. Technol. 108 (2022) 226–235, https://doi.org/10.1016/j.jmst.2021.07.059.
[42] G. Di Egidio, L. Ceschini, C. Martini, A. Morri, Influence of Ni-P + DLC multilayer coatings on the tensile properties of the AlSi10Mg alloy produced by laser-based powder bed fusion, Proc. Struct. Integr. 47 (2023) 337–347, https://doi.org/10.1016/J.PROSTR.2023.07.091.
[43] E. Lugscheider, G. Krämer, C. Barimani, H. Zimmermann, PVD coatings on aluminium substrates, Surf. Coat. Technol. 74–75 (1995) 497–502, https://doi.org/10.1016/0257-8972(95)08305-7.
[44] E. Cerri, E. Ghio, M. Cabibbo, Gradient of precipitation phenomena in tall laser powder bed-fused AlSi7Mg samples: effects of heated substrate and aging heat treatments, J. Alloys Compd. 1020 (2025) 179459, https://doi.org/10.1016/j.jallcom.2025.179459.
[45] V.D.I. Normen, VDI 3198, VDI-Verlag (1991) 1–8.
[46] E. Ogris, A. Wahlen, H. Lüchinger, P.J. Uggowitzer, On the silicon spheroidization in Al–Si alloys, J. Light. Met. 2 (2002) 263–269, https://doi.org/10.1016/S1471-5317(03)00010-5.
[47] E. Cerri, E. Ghio, Metallurgical analysis of laser powder bed-fused Al–Si–Mg alloys: Main causes of premature failure, Mater. Sci. Eng. A 881 (2023) 145402, https://doi.org/10.1016/j.msea.2023.145402.
[48] E. Cerri, E. Ghio, G. Bolelli, Effect of the distance from build platform and post-heat treatment of AlSi10Mg alloy manufactured by single- and multi-laser selective laser melting, J. Mater. Eng. Perform. 30 (2021) 4981–4992, https://doi.org/10.1007/s11665-021-05577-8.
[49] L. Tonelli, E. Liverani, A. Morri, L. Ceschini, Role of direct aging and solution treatment on hardness, microstructure and residual stress of the A357 (AlSi7Mg0.6) alloy produced by powder bed fusion, Metall. Mater. Trans. B Process Metall. Mater. Process. Sci. 52 (2021) 2484–2496, https://doi.org/10.1007/s11663-021-02179-6.
[50] J. Mei, Y. Han, J. Sun, M. Jiang, G. Zu, X. Song, W. Zhu, X. Ran, Improving the comprehensive mechanical property of the AlSi10Mg alloy via parameter adaptation of selective laser melting and heat treatment, J. Alloys Compd. 981 (2024) 173623, https://doi.org/10.1016/j.jallcom.2024.173623.
[51] G. Di Egidio, L. Tonelli, M. Zanni, D. Carosi, A. Morri, L. Ceschini, Direct artificial aging of the PBF-LB AlSi10Mg alloy designed to enhance the trade-off between strength and residual stress relief, J. Alloys Metall. Syst. 5 (2024) 100063, https://doi.org/10.1016/j.jalmes.2024.100063.
[52] J.A. Greenwood, J.B.P. Williamson, Contact of nominally flat surfaces, Proc. R. Soc. Lond. A Math. Phys. Sci. 295 (1966) 300–319, https://doi.org/10.1098/rspa.1966.0242.
[53] W. Österle, D. Klaffke, M. Griepentrog, U. Gross, I. Kranz, C. Knabe, Potential of wear resistant coatings on Ti–6Al–4V for artificial hip joint bearing surfaces, Wear 264 (2008) 505–517, https://doi.org/10.1016/J.WEAR.2007.04.001.
[54] B.D. Beake, T.W. Liskiewicz, V.M. Vishnyakov, M.I. Davies, Development of DLC coating architectures for demanding functional surface applications through nano- and micro-mechanical testing, Surf. Coat. Technol. 284 (2015) 334–343, https://doi.org/10.1016/J.SURFCOAT.2015.05.050.
[55] C. Wei, K.S. Peng, M.S. Hung, The effect of hydrogen and acetylene mixing ratios on the surface, mechanical and biocompatible properties of diamond-like carbon films, Diam. Relat. Mater. 63 (2016) 108–114, https://doi.org/10.1016/J.DIAMOND.2015.10.031.
[56] Z. Su, X. Jie, W. Li, Z. Liao, Y. Li, W. Zhu, Effect of C2H2 flow rate and a Ti/TiN/TiCN interlayer on the structure, mechanical and tribological properties of a-C:H films deposited using a hybrid PVD/PECVD process with an anode-layer ion source, Vacuum 209 (2023) 111753, https://doi.org/10.1016/J.VACUUM.2022.111753.
[57] T. Kasiorowski, J. Lin, P. Soares, C.M. Lepienski, C.A. Neitzke, G.B. de Souza, R. D. Torres, Microstructural and tribological characterization of DLC coatings deposited by plasma enhanced techniques on steel substrates, Surf. Coat. Technol. 389 (2020) 125615, https://doi.org/10.1016/J.SURFCOAT.2020.125615.
[58] A.C. Ferrari, J. Robertson, Interpretation of Raman spectra of disordered and amorphous carbon, Phys. Rev. B 61 (2000) 14095–14107, https://doi.org/10.1103/PhysRevB.61.14095.
[59] A. Singha, A. Ghosh, A. Roy, N.R. Ray, Quantitative analysis of hydrogenated diamondlike carbon films by visible Raman spectroscopy, J. Appl. Phys. 100 (2006) 1–20, https://doi.org/10.1063/1.2219983.
[60] B. Marchon, K. Jing Gui, G.C. Grannen, J.W. Rauch, S.R.P. Ager, J. Robertson Silva, Photoluminescence and Raman spectroscopy in hydrogenated carbon films, IEEE Trans. Magn. 33 (1997) 3148–3150, https://doi.org/10.1109/20.617873.
[61] C. Casiraghi, A.C. Ferrari, J. Robertson, Raman spectroscopy of hydrogenated amorphous carbons, Phys. Rev. B 72 (2005) 085401, https://doi.org/10.1103/PhysRevB.72.085401.
[62] E. Cerri, E. Ghio, On the work-hardening behaviour of the additively manufactured Al-Si-Mg alloys: composite-like versus networked microstructure, Materialia (Oxf) (2024) 102282, https://doi.org/10.1016/j.mtla.2024.102282.
[63] G. Straffelini, Friction, in: Friction and Wear - Methodologies for Design and Control, Springer International Publishing, Cham, Switzerland, 2015, pp. 21–60, https://doi.org/10.1007/978-3-319-05894-8_2.
[64] K.C. Ludema, O.O. Ajayi, Friction, Wear, Lubrication, Second ed., Taylor & Francis, CRC Press, Boca Raton, FL, USA, 2018 https://doi.org/10.1201/9780429444715.
[65] K. Kato, K. Adachi, Wear mechanisms, in: B. Bhushan (Ed.), Modern Tribology Handbook 1, CRC Press, Boca Raton, FL, USA, 2001, pp. 273–300.
[66] S.J. McMaster, S. Kosarieh, T.W. Liskiewicz, A. Neville, B.D. Beake, Utilising H/E to predict fretting wear performance of DLC coating systems, Tribol. Int. 185 (2023) 108524, https://doi.org/10.1016/J.TRIBOINT.2023.108524.
[67] N.T. Aboulkhair, N.M. Everitt, I. Ashcroft, C. Tuck, Reducing porosity in AlSi10Mg parts processed by selective laser melting, Addit. Manuf. 1–4 (2014) 77–86, https://doi.org/10.1016/J.ADDMA.2014.08.001.
[68] W. Tillmann, N.F. Lopes Dias, D. Stangier, C. Schaak, S. Höges, Coatability of diamond-like carbon on 316L stainless steel printed by binder jetting, Addit. Manuf. 44 (2021) 102064, https://doi.org/10.1016/j.addma.2021.102064.